Petrology, Vol. 5, No. 6, 1997, pp. 503–533. Translated from Petrologiya, Vol. 5, No. 6, 1997, pp. 563–595.

Petrology of the Tumanshet Zonal Metamorphic Complex, Eastern Sayan

T. V. Gerya*, L. L. Perchuk*, C. Triboulet, C. Audren***, and A. I. Sez'ko******

** Institute of Experimental Mineralogy, Russian Academy of Sciences, Chernogolovka, Moscow oblast, 142432 Russia; e-mail: alp@p1854.home.chg.ru*

*** Laboratoire de Petrologie et Mineralogique, C.N.R.S., U.R.A. 736, Universite Pierre et Marie Curie, 4 place Jussieu, F-75252 Paris, Cedex 05, France; e-mail: clt@ccr.jusseu.fr*

**** Geosciences Rennes Laboratoire et Tectonophysique, Institute de Geologie, Avenue du General Leclere, F-35042, Rennes Cedex, France; e-mail: aifa@seth.univ-rennes 1.fr*

***** Institute of the Earth's Crust, Siberian Division, Russian Academy of Sciences, ul. Lermontova 128, Irkutsk, 664033 Russia*

Received March 30, 1997

Abstract—The Tumanshet Complex fills a Proterozoic basin and rests with stratigraphic unconformity on the boundary between an Early Precambrian greenstone belt and the migmatite–granulite complex of the Siberian craton. Petrographic study revealed metamorphic zonation in the Tumanshet Complex. The thermobarometry of mineral equilibria based on the zoning of coexisting minerals locates temperature (up to 680°C) and pressure (up to 7 kbar) maxima in the central part of the basin. On the geological map, these maxima coincide with the gravity step which marks the deep-seated fault separating the greenstone belt and migmatite–granulite complex. The formation of the deep basin on this boundary is related to the influence of mantle plumes in the Proterozoic (~1750 Ma).

INTRODUCTION

Relationships between granulites and greenstone complexes have long drawn the close attention of petrologists. It was primarily caused by the lack of models of geological correlation for these complexes and common tectonic contacts between them. Only recent concepts connected geodynamic and structural features of the evolution of these complexes (Perchuk, 1989a, 1991; Perchuk *et al.*, 1996). In the early 1960s, Pavlovskii (1962) proposed the genetic relation of these complexes, and 25 years later Petrova and Levitskii (1984) found evidence of geochemical similarity of these apparently different complexes. Numerical hydrodynamic modeling showed (Perchuk *et al.*, 1992) that the origin of paired metamorphic belts of the granulite–craton (granite–greenstone belts) type could result from gravitational mass redistribution within rhythmically layered volcanogenic–sedimentary complexes due to significant thermal excitement of the lower crust by mantle diapirs. The rate of this process is mainly controlled by rhythmical intercalation of primary deposits in a given complex.

The common and, moreover, subsequent history of these spatially related complexes has never been studied. However, many publications reported the results of investigation of so-called superimposed cratonic basins with well-developed metamorphic zonation. They bear information on the late thermal and geodynamic history of genetically related mafic greenstone belts and sialic granite gneisses, granulites and migmatites. A remarkable example of such basins is the junction of the Sayan Shield of the Siberian craton with the Early Precambrian greenstone complexes of the Central Asian foldbelt (Sez'ko, 1990, 1997). It coincides with a suture zone of positive gravity anomalies, which correspond to basic and ultrabasic masses in higher levels of the crust. The basement of the Siberian craton adjacent to the suture zone is composed of uniform sialic migmatite, gneiss and granulite complexes.

The aim of this study is to reconstruct the tectonic and thermodynamic conditions of formation of metamorphic rocks from the Tumanshet basin and to work out a geodynamic model for complex evolution. Field work was undertaken to solve two geological problems:

(1) To determine the evolution of metamorphic parameters and rock deformation in different metamorphic zones of the basin and within the basement;

(2) To compare the metamorphic and deformation features of rocks from the zonal complex and the basement (at unconformity between the Archean and Proterozoic).

In order to solve these problems, a 70-km long cross section along the Tumanshet River (Fig. 1) was sampled. About 100 samples of rocks with different mineral and chemical composition were collected regularly; each outcrop was studied in detail structurally. It allowed us to outline the structural pattern of the region and distinguish the deformation sequence during the geodynamic evolution of the complex.

One-third of the 100 collected samples were informative (Table 1); ten were used in the detailed study. Polished thin sections of the rocks cut across schistosity and along lineation were studied by the well-developed methods of microstructural and paragenetic analysis along with geothermobarometry (Audren and Triboulet, 1993).

GEOLOGIC SETTING OF THE COMPLEX

Along the geological traverse from the Yenisei Range to the southwestern Baikal area (Sez'ko, 1990, 1997), three structural units are distinguished: the Early Precambrian East Siberian greenstone belt, the Sayan Shield of the Siberian craton, and the Early Proterozoic basins superimposed on the contacts of the two first units. Early Archean age of the sialic complex of the Sayan Shield is supported by isotopic dating of tonalites containing zircons with an U–Pb age of 3250 ± 100 Ma (Bibikova *et al.*, 1982). These sialic complexes form a basement for the Archean mafic greenstone belts: Monkress, Targazoi, Tagul, etc. The evolution of metamorphic rocks of the basins terminated in the end of the Early Proterozoic, as indicated by the Pb–Pb zircon dating of tourmaline-bearing granites, which intruded the Tumanshet Formation 1730 Ma ago (Bryntsev *et al.*, 1985).

The Tumanshet basin was formed at the contact of the Malyi Tagul greenstone belt and high-grade rocks of the Biryusa block of the Sayan Shield. Sez'ko (1988) observed stratigraphic and structural unconformities between amphibolites and gneisses of the Monkress Group of the Malyi Tagul greenstone belt and basal arkose gravelites and sandstones of the Tumanshet basin. This suggests Archean age for the Malyi Tagul greenstone belt, because the overlying rocks of the Tumanshet basin are Early Proterozoic. The Tumanshet basin is situated in the northwesten part of the Biryusa zone of the eastern Sayan, between the Tagul and Tumanshet rivers (Fig. 1). It is part of the elongated zone of Proterozoic basins formed on the Archean basement of the Biryusa zone. The initial lithology of the Tumanshet basin included Proterozoic quartzites, sandstones, siltstones, shales, graywakes, and carbonate rocks metamorphosed under *P–T* gradient conditions. It resulted in well-developed metamorphic zonation of the basin from greenschist to amphibolite facies. The latest evolution stage at 1730 Ma (Bryntsev *et al.*, 1985) was manifested by small intrusions of tourmaline–biotite–muscovite granites.

RESULTS

Structural–petrologic study. The discovery (Sez'ko, 1988) of structural and stratigraphic unconformity between the Archean and Proterozoic rocks gave rise to a problem as to the extent in which the rocks underlying the southwestern granite–greenstone complex and the northeastern gneisses were affected by later deformations and metamorphism. In order to clarify it, a detailed structural–petrologic study was undertaken.

Paragenetic associations distinguished in thin sections present mineral generations which were formed simultaneously during some deformation stages within a narrow range of temperature and pressure. They may correspond to a single metamorphic subfacies or even facies within which *P* and *T* change regularly. Such associations are divariant, and changing metamorphic conditions result in compositional change of coexisting minerals within divariant fields. Deformations activate this process owing to more intense percolation of metamorphic fluid in the rocks. The paragenetic analysis of minerals in the divariant fields includes microprobe study followed by the thermobarometry of the revealed generations. As a result, information on the conjugated evolution of *P–T* metamorphic conditions and deformation features, i.e. folding, schistosity, and lineation, may be obtained.

The generalized results of the structural study are shown on Fig. 2. The structures of the first deformation cycle, D1, are the most common within the *zoned* complex. They are represented by lineation (L1) and schistosity (S1). Folding P1 is weaker. The lineation (L1) is marked by the shapes and elongation of pressure shadows around garnet grains and by the orientation of chlorite and biotite grains parallel to the P1 fold axes. Two other deformation stages, D2 and D3, were distinguished. The second deformation resulted in the information of small folds after schistosity S1. Deformation D3 forms normally large box folds whose axes are often parallel to plication P2. Megastructures D3 are well marked by layers of carbonate–silicate rocks. Figure 2 shows the identical orientations of the axes of synform D3 (1, 2) and antiform D3 (3).

The structural scheme of the Archean basement (F) differs completely from that of the Tumanshet Complex. The schistosities and lineations of both complexes are discordant. The lineations of the basement rocks is meridional, whereas in the zonal complex, it strikes from northwest to southeast (Fig. 2). Late folding P3 is overprinted on the earlier schistosity S1F and lineation L1F. Possibly, this folding is common for both the basement and the zonal complex. Earlier tectonic and metamorphic events in the zonal complex and the basement proceeded independently, and thermodynamic and structural evolutions of the complexes were different. The complexes were evidently formed during different cycles of deformations (D1F and D1).

The obtained results of the structural study could be regarded as indicating that the Archean and Proterozoic parts were combined only on the final stage of their tectonic and metamorphic history. In this case, the premetamorphic unconformity in the rocks of the zonal complex would be tectonically displaced respective to the Archean basement. However, there is an alternative solution based on the fact that the Tumanshet Complex underwent zonal metamorphism, and the highest parameters were reached in its central parts. The metamorphic grade decreases to phyllites and almost unmetamorphosed arkose sandstones toward the basement contact. In such a geologic environment, the secondary schistosity and lineation related to the metamorphism and deformations of plastic sedimentary rocks of the Pro-

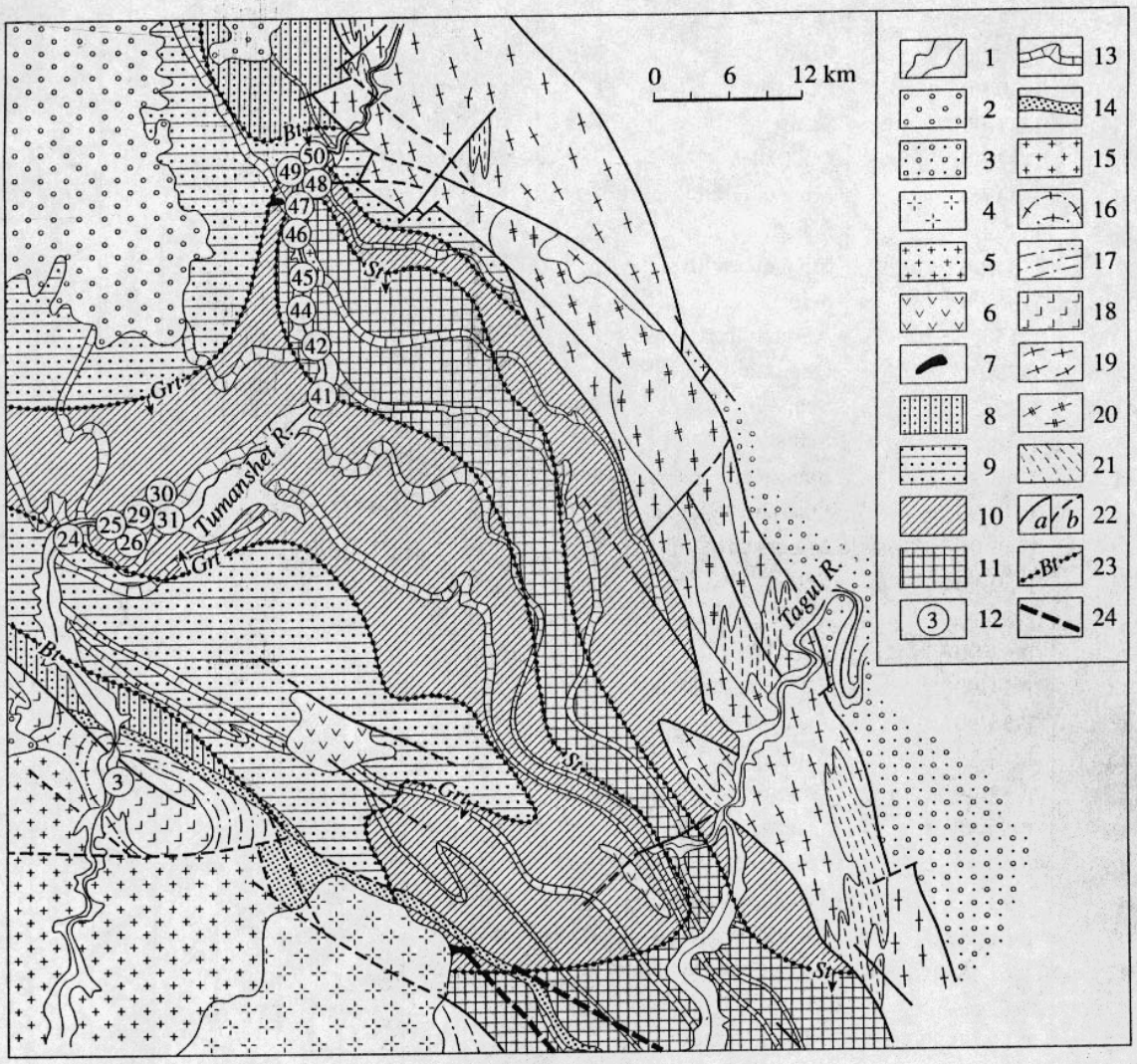

Fig. 1. Scheme of metamorphic zonation of the Tumanshet basin, superimposed on the Archean basement (Sez'ko , 1988).
(1) Quaternary deposits of the Tagul and Tumanshet River valleys; (2) Devonian unmetamorphosed deposits; (3) Late Proterozoic unmetamorphosed deposits, Karagass Group; (4) Paleozoic subalkaline granites, granosyenites (Ognitskii Complex); (5) Early Proterozoic granitoids (Sayan Complex); (6) Early Proterozoic metadiabases, orthoamphibolites, gabbro, metagabbro; (7) Early Proterozoic ultramafic and metaultramafic rocks (Idarskii Complex); (8–11) zones of regional metamorphism of metapelites and peraluminous schists of the Early Proterozoic Neroyskaya Group: (8) pre-biotite, (9) biotite, (10) garnet, (11) staurolite; (12) outcrop numbers; (13) layers of limestones and marbles of the Early Proterozoic Neroyskaya Group; (14) basal quartzite layer of the Tumanshet Formation; (15) undifferentiated Early Proterozoic–Late Archean granitoids; (16) Late Archean migmatites, granitogneisses; (17, 18) amphibolite facies in rocks of the Late Archean Monkress Group: (17) leucocratic biotite gneisses, granitogneisses, (18) amphibolites, garnet amphibolites; (19) undifferentiated Early–Late Archean granitogneisses, migmatites of the Khadaminskii (Onot, Kitoi) Complex; (20) Archean enderbites and charnockite rocks; (21) granitized granulites of the Early Archean Khailaminskaya Group; (22) (*a*) observed and (*b*) inferred faults; (23) metamorphic isograde; (24) earlier accepted boundary of the Tumanshet graben (Sez'ko, 1988).

terozoic Tumanshet basin could not be developed in the cold and rigid rocks of the Archean basement.

Microstructural Study

Zonal complex. Table 1 shows that the *metapelites* are mainly composed of quartz, plagioclase, muscovite/paragonite, chlorite, chloritoid, biotite, garnet, tourmaline, and staurolite, whereas the *metabasites* are composed of amphibole, chlorite, epidote, plagioclase, and carbonate. Aluminum silicates were not found in any of the samples. Three isograde were distinguished on the basis of mineral parageneses in the metapelites (Sez'ko, 1988): biotite, garnet, and staurolite. They reflect temperature increase toward the center of the Tumanshet Complex but do not provide information on the evolution of thermodynamic parameters of metamor-

Table 1. Mineral associations of the studied rocks from the Tumanshet zonal complex

Outcrop number	Sample number	Rock	*Grt*	*Chl*	*Bt*	*St*	*Cld*	*Ep*	*Ms*	*Kfs*	*Hbl*	*Cpx*	*Cal*
3	T-3 (basement)	Amphibolite	+	+	–	–	–	+	–	–	+	+	+
24	T-13	Mica quartzite	–	+	–	–	–	–	+	–	–	–	–
24	T-27-90	Quartzite	–	+	–	–	–	–	+	–	–	–	–
24	T-28-90	Quartzite	–	+	–	–	–	–	+	–	–	–	–
25	T-30-90/1*	Schist	+	+	+	–	–	–	+	–	–	–	–
25	T-30-90/2*	Quartzite	+	+	–	–	–	–	+	–	–	–	–
25	T-31-90	Schist	+	+	+	–	–	–	+	–	–	–	–
26	T-32-90	Quartzite	+	+	+	–	+	–	+	–	–	–	–
26	T-33-90	Mica quartzite	+	+	–	–	–	–	+	–	–	–	–
29	T-14a	Schist	+	+	–	–	–	+	+	–	–	–	–
29	T-34-90	Mica quartzite	+	+	–	–	–	–	+	–	–	–	–
29	T-35-90	Schist	+	+	–	–	–	+	–	+	–	–	–
30	T-15	Amphibolite	–	–	+	–	–	+	–	–	+	–	+
31	T-39-90	Quartzite	+	+	+	–	–	–	+	–	–	–	–
41	T-17	Schist	+	+	+	+	–	–	+	–	–	–	–
41	T-45-90	Schist	+	+	+	+	–	–	+	–	–	–	–
41	T-46-90	Schist	+	+	+	+	–	–	+	–	–	–	–
42	T-48-90	Quartzite	+	+	+	–	–	–	+	–	–	–	–
42	T-49-90	Mica quartzite	+	–	+	–	–	–	+	–	–	–	–
42	T-50-90	Schist	+	+	–	–	–	–	–	+	–	–	–
42	T-51-90	Schist	+	+	+	–	–	–	–	+	–	–	–
44	T-53-90	Schist	+	+	–	+	–	–	–	+	–	–	–
44	T-54-90	Mica quartzite	+	+	–	+	–	–	–	+	–	–	–
44	T-55-90	Quartzite	–	+	–	+	–	–	–	+	–	–	–
44	44	Mica quartzite	+	+	–	+	–	–	–	+	–	–	–
45	T-58-90/1*	Granite	–	+	+	–	–	–	–	+	–	–	–
45	T-58-90/2*	Quartzite	+	–	+	–	–	–	+	+	–	–	–
46	T-60-90	Quartzite	+	–	+	–	–	–	+	+	–	–	–
47	T-23	Mica quartzite	+	+	–	–	+	–	+	–	–	–	–
47	T-61-90/1*	Quartzite	+	+	+	–	–	–	+	–	–	–	–
47	T-61-90/2*	Mica quartzite	+	+	–	–	+	–	+	–	–	–	–
47	T-62-90/1*	Quartzite	+	+	+	–	–	–	+	–	–	–	–
47	T-62-90/2*	Mica quartzite	+	+	–	–	+	–	+	–	–	–	–
47a	T-64-90	Schist	+	+	+	–	–	–	+	–	–	–	–
47a	T-65-90	Schist	+	+	+	–	+	–	+	–	–	–	–
48	T-66-90	Mica quartzite	+	+	–	–	+	–	+	–	–	–	–
48	T-67-90	Schist	–	+	–	–	–	–	+	–	–	–	–
49	T-25a/1*	Mica quartzite	+	+	–	–	+	–	+	–	–	–	–
49	T-25a/2*	Mica quartzite	+	+	–	–	+	–	+	–	–	–	–
49	T-25b	Amphibolite	–	–	+	–	–	+	–	–	+	–	+
49	T-68-90	Mica quartzite	+	+	–	–	+	–	+	–	–	–	–
50	T-69-90	Schist	+	+	+	–	–	–	+	–	–	–	–
50	T-70-90	Quartzite	+	+	+	–	+	–	+	–	–	–	–

Note: All the samples contain quartz and plagioclase.

* Different laminas within single sample.

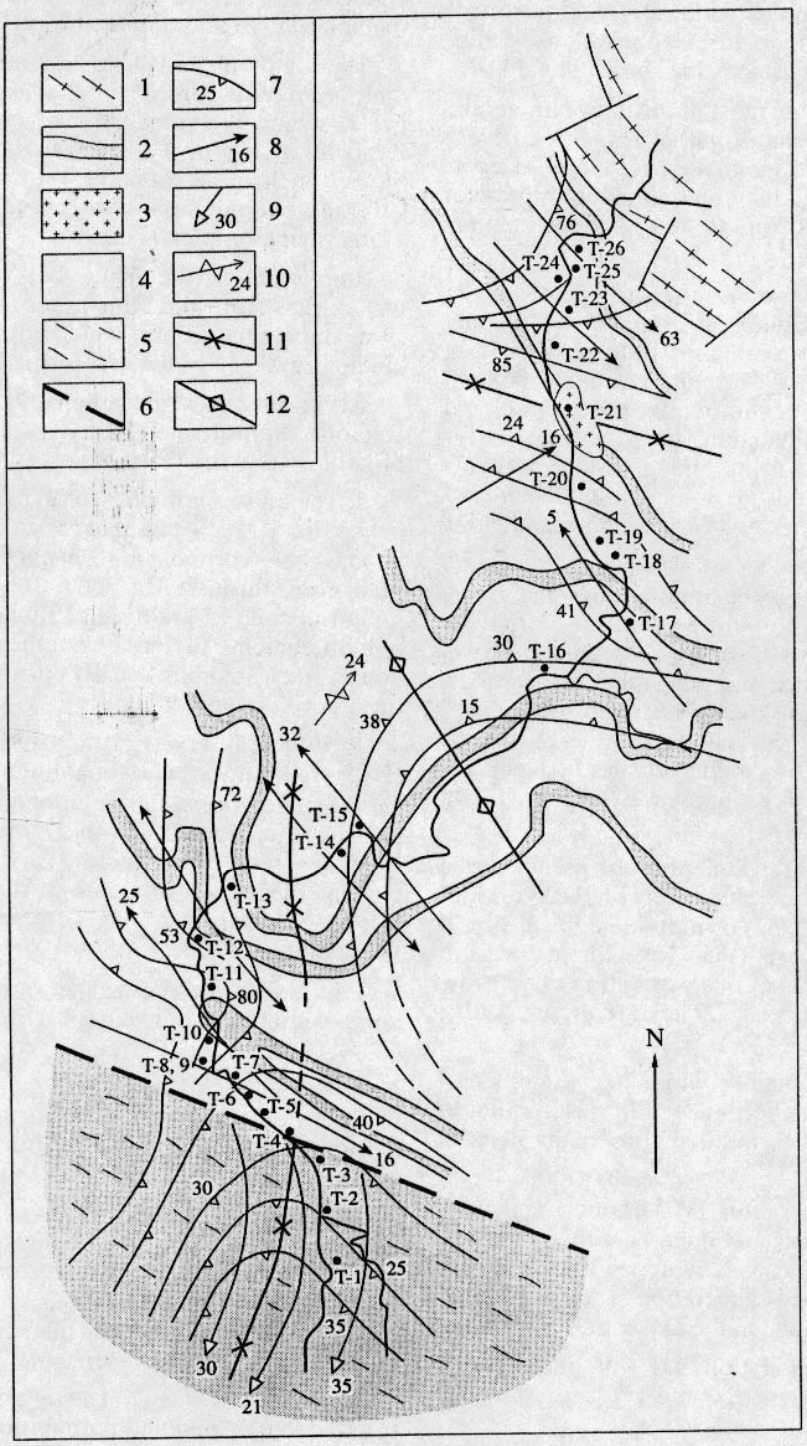

Fig. 2. Structural and geological scheme of the Tumanshet basin along the Tumanshet River.
(1) Archean granitoids; (2) carbonate layers; (3) granites; (4) rocks of the Tumanshet basin; (5) Archean greenstone belt; (6) structural unconformity between the greenstone belt and the Tumanshet basin; (7) strike and dip angle of the D1 schistosity; (8) orientation of lineation in rocks of the Tumanshet Complex; (9) orientation of lineation in rocks of the greenstone belt; (10) orientation of fold axes of kinematic cycle D2 within the Tumanshet Complex; (11) large synforms of deformation cycle D3; (12) large antiforms D3.

phism. Since no reaction textures occur in the rocks, the correct solution of the problem is possible only with microstructural data.

Only microstructures of the first cycle of deformations, D1, were observed in thin sections of rocks from the zonal complex. However, the detail study showed prekinematic ($D1_0$), synkinematic ($D1_s$) and postkinematic ($D1_p$) mineral generations. Compositions of minerals from different generations are shown in Table 2.

Garnet is one of the most informative minerals. Three distinct generations of garnet (Figs. 3–5) were recognized. Within postkinematic generation $D1_p$, retrograde generation $D1_{p^*}$ may be defined with mineral compositions corresponding to retrograde metamorphism.

1. Prekinematic generation $D1_0$ forms cores of the largest garnet porphyroblasts surrounded by distinct pressure shadows in the samples of mica schists from different zones (Fig. 3a). The porphyroblasts contain numerous small inclusions of quartz, plagioclase, and ilmenite of random orientation; they show low Mg-number and high spessartine and grossular contents (Fig. 4). This generation is predominant in the cores of garnet (Figs. 3b, 3d, 5a, 5b) formed during the D1 deformation.

2. Synkinematic ($D1_s$) generation either overgrows the prekinematic garnet or forms separate porphyroblasts surrounded by distinct pressure shadows (Figs. 3a, 3b, 3d) in schist and mica quartzite samples. Garnet of this generation is characterized by oriented quartz and plagioclase inclusions forming S-shaped structures (Fig. 3b). Compared with the first generation, this garnet is always significantly higher in Mg and lower in Mn (Fig. 4).

3. Postkinematic ($D1_p$) generation of garnet forms either fragmentary idiomorphic facets on the syn-kinematic ($D1_s$) garnet (Fig. 3a) or individual small (up to 0.3 mm) euhedral crystals (Fig. 3c) without pressure shadows. Garnet crystals of this generation often grow across schistosity S1 (Fig. 3c). They are the most Mg-rich and Mn-poor (Fig. 4).

Phyllosilicates are mainly white micas and chlorites. Biotite is usually subordinate (Table 1). Similar to garnets, phyllosilicates form three consequent generations.

1. Prekinematic generation ($D1_0$) of micas and chlorites occurs in the schists and mica-bearing quartzites. It forms microlenses and pods wrapped by schistosity S1 (Fig. 3a). Locally, this generation is found in large quartz–feldspar inclusions in the $D1_0$ garnet.

2. Synkinematic generation ($D1_s$) of micas forms schistosity S1 in rock matrix and pressure shadows around garnets (Fig. 3a).

3. Postkinematic generation ($D1_p$) of micas forms elongated euhedral grains (Fig. 3c), crosscutting $D1_s$ structures, or locally replaces garnet rims (Fig. 3d).

Figure 6 shows variations of muscovite and paragonite compositions in the rocks of the Tumanshet zonal complex at different stages of the main kinematic cycle, D1. The first diagram (a) demonstrates that the Al : Si ratio in micas increases and muscovite and phengite contents decrease as Al content of octahedra decreases. These changes are related to a temperature change during metamorphism and deformations (Fig. 6b).

The Mg-number of chlorites correlates negatively with their aluminum content on any stage of the kinematic cycle, which is typical of metapelites (Perchuk and Ryabchikov, 1976, p. 94). It is demonstrated (Fig. 7a) by two metapelite Samples T-14 and T-17 (Table 1). Chlorite composition changes regularly across the Tumanshet Complex (Fig. 7b).

Amphibole is the main rock-forming mineral of metabasites from the Tumanshet zonal complex. They show three generations, which correlate with the three kinematic stages of mineral formation in metapelites.

1. Prekinematic generation ($D1_0$) is represented by actinolite hornblende (Table 3) forming usually cores of large synkinematic grains.

2. The most common is the synkinematic amphibole generation ($D1_s$). Actinolite crystals form the rock foliation. Their composition changes from actinolite in grain cores through Mg-rich hornblende to tschermakite hornblende in grain rims (Table 3). Alkali and aluminum contents increase from the center to the rim of grains. Such a zoning usually corresponds to increasing metamorphic temperature.

3. Euhedral crystals of postkinematic amphibole ($D1_p$) crosscut the rock foliation or overgrow grains of earlier generations. Their composition changes from tschermakite hornblende in grain centers to Mg-rich hornblende in rims (Table 3). Alkali and aluminum contents decrease from core to rim. In contrast to the $D1_s$ stage, such a zoning corresponds to decreasing temperature.

Figure 8 shows the regular variations of amphibole composition in two metabasites during deformations.

Plagioclase. Three plagioclase generations were identified in each rock. These generations correspond to three mineral-forming stages of the first cycle of deformations (Table 3). Anorthite content of plagioclase increases from the earlier to later generations.

Basement. The basement is composed of garnetiferous and garnet-free amphibolites. Amphibole, garnet, plagioclase, and clinopyroxene are the main rock-forming minerals. Two generations of minerals, synkinematic ($D1F_s$) and postkinematic ($D1F_p$), are distinguished in the rocks.

Garnets of the synkinematic generation form large (up to 1 cm) elongated porphyroblasts surrounded by distinct pressure shadows. They contain numerous inclusions of amphibole and rare clinopyroxene (Fig. 3e) oriented at an angle of ~30° to the rock folia-

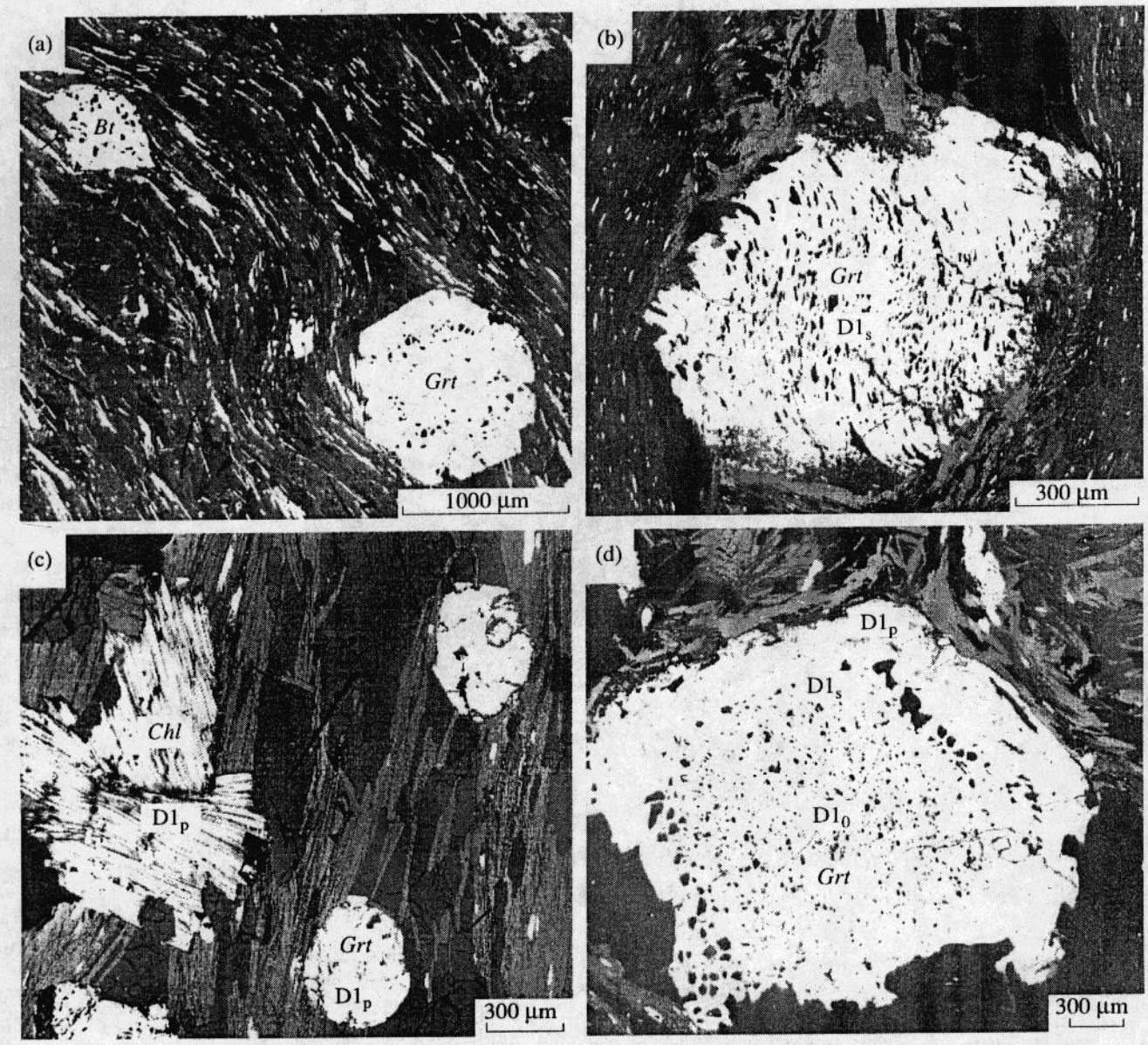

Fig. 3. Deformational features of metamorphism in the Tumanshet basin (a–d) and underlying rocks of the greenstone belt (e–g).
(a) Pressure shadows formed during garnet and biotite pod growth during deformation cycle D1. Mica minerals form schistosity S1, Sample T-64-90; (b) deformed ($D1_s$) garnet with oriented inclusions of *Qtz* and *Ilm* in Sample T-31-90; (c) postkinematic ($D1_p$) generations of garnet and chlorite cutting schistosity S1, Sample T-50-90; (d) garnet core ($D1_0$) with disoriented inclusions of *Qtz* and *Ilm*, locally overgrown by syn- ($D1_s$) and post-kinematic zones ($D1_p$) in Sample T-17; (e) garnet porphyroblasts containing *Hbl*, *Cpx*, and *Pl* inclusions from rocks of the greenstone belt, underlying the Tumanshet zonal complex, Sample T-3; first kinematic cycle D1F in the basement rocks; (f) postkinematic generation of garnet ($D1F_p$) formed in hornblende grain and surrounded by plagioclase corona, Sample T-3; (g) secondary generation of amphibole (*Hbl*-2, $D1F_{p*}$) replacing primary ($D1F_s$, $D1F_p$) hornblende (*Hbl*-1) and garnet (*Grt*) generations along cracks, Sample T-3.

tion. The Mg-number of the synkinematic garnets decreases from cores to rims of grains (Fig. 9). The composition of amphibole and clinopyroxene inclusions also changes from core to rim of the porphyroblasts (Fig. 9).

Postkinematic garnet forms thin (~100 μm) relatively high-Mg rims around synkinematic porphyroblasts (Fig. 3e), as well as small rounded homogeneous grains in the matrix. This garnet is not stable with hornblende, and these minerals are always separated by plagioclase corona (Fig. 3f, Table 3).

Synkinematic amphiboles and clinopyroxenes form the matrix and most of the inclusions in garnet. They are extended along the *c*-axis and well-oriented marking S1F and D1F microstructures in the rocks, including pressure shadows around the garnet porphyroblasts. The compositions of the synkinematic amphibole changes from ferrotschermakite hornblende to Mg-rich hornblende (Table 3). Postkinematic clinopyroxene and

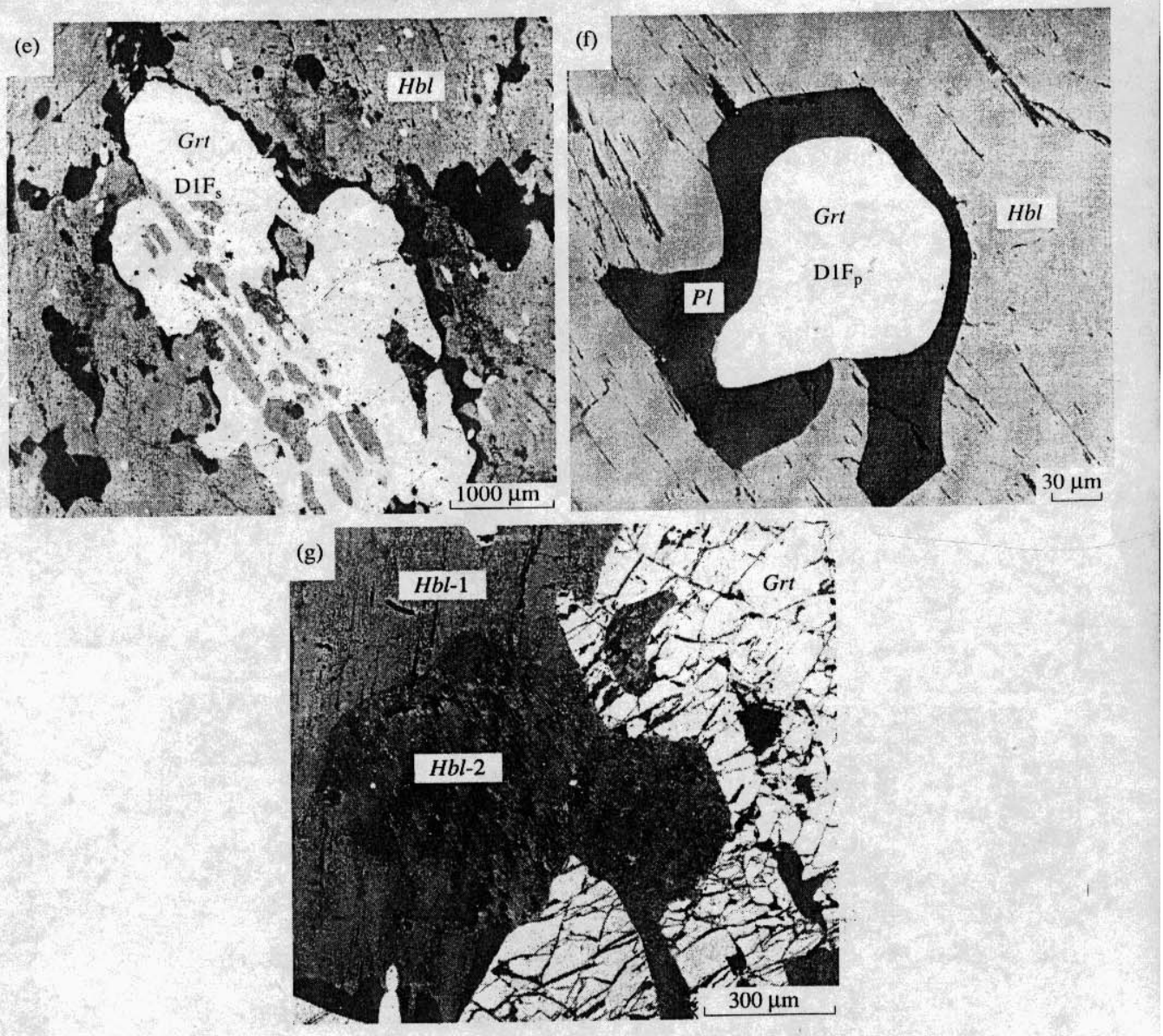

Fig. 3. (Contd.)

amphibole form small grains. They replace the synkinematic generations of *Hbl*[1] and *Cpx* (Fig. 3g) and form secondary inclusions in the garnet porphyroblasts. Compared with the earlier generation, these newly-formed minerals are appreciably richer in Fe (Fig. 9, Table 2). The post-kinematic amphibole is chemically actinolite hornblende or actinolite (Table 2).

Large synkinematic plagioclase grains are distinctly zoned. Their composition changes from $An_{31}Ab_{69}$ in the centers to $An_{40}Ab_{60}$ in the rims of grains. Small postkinematic plagioclase is unzoned and its composition is similar to that of the rims of large synkinematic grains.

Mineral Growth and Mineral Reactions

As was noted above, the rocks of the zonal complex are essentially devoid of reaction textures. The only exceptions are thin (5–10 μm) coronas of *Chl* + *Ms* +

[1] *Mineral symbols*: *Ab*, albite; *Act*, actinolite; *Alm*, almandine; *Ams*, amesite; *An*, anorthite; *Bt*, biotite; *Cal*, calcite; *Chl*, chlorite; *Cln*, clinochlore; *Cld*, chloritoid; *Cpx*, clinopyroxene; *East*, eastonite; *Ed*, edenite; *Ep*, epidote; *Grs*, grossular; *Grt*, garnet; *Hbl*, hornblende; *Ilm*, ilmenite; *Kfs*, K-feldspar; *Ms*, muscovite; *Par*, pargasite; *Pg*, paragonite; *Phg*, phengite; *Phl*, phlogopite; *Pl*, plagioclase; *Prp*, pyrope; *Qtz*, quartz; *Sps*, spessartine; *St*, staurolite; *Tr*, tremolite; *Tsc*, tschermakite; *Zo*, zoisite.
Thermodynamic symbols and functions: *T*, temperature; *P*, pressure; ΔG^0, ΔH^0, ΔS^0, and ΔV^0 are change in standard state Gibbs free energy, enthalpy, entropy, and volume, respectively, in mineral reaction; X_i is mole fraction of component *i* in solution; X^{α}_{Mg} = Mg/(Mg + Fe) is Mg mole fraction in a mineral or system; $\alpha_i = \gamma_i X_i$, activity of component *i* in a mineral; γ_i, activity coefficient of component *i* in solution.

Table 2. Selected microprobe analyses and crystallochemical formulas of coexisting minerals in the studied samples (wt %)

Components	T-3 (basement)															T-31-90	
	$D1F_s$				$D1F_s$		$D1F_s$		$D1F_p$		$D1F_p$			$D1F_p$		$D1F_s$	
	Grt	*Hbl*	*Pl*	*Cpx*	*Grt*	*Hbl*	*Grt*	*Hbl*	*Grt*	*Hbl*	*Grt*	*Hbl*	*Pl*	*Hbl*	*Pl*	*Grt*	*Chl*
	D20/1*c***	D32	D41	S1	D22/1*i*	D23	D18/1*r*	D30	D17/1*m*	D31	S52/2*c*	S55	S56	S4	S6	W1/1*c*	W16
SiO_2	38.35	44.54	59.98	52.08	38.33	44.14	38.44	42.67	37.97	48.56	38.24	44.01	56.63	41.34	60.01	37.03	28.33
TiO_2	0.14	1.10	0.00	0.19	0.10	1.23	0.11	0.22	0.11	0.54	0.28	1.21	0.00	0.07	0.00	0.00	0.09
Al_2O_3	20.85	12.82	24.73	2.26	20.80	14.20	20.94	13.08	21.25	7.48	20.92	13.06	26.84	15.94	24.72	20.96	25.05
FeO	21.90	16.89	0.08	10.54	22.35	17.37	21.88	22.28	22.56	20.20	22.84	17.49	0.35	22.47	0.45	30.26	26.90
MnO	2.46	0.22	0.00	0.25	1.91	0.14	2.01	0.31	1.85	0.49	1.17	0.19	0.00	0.36	0.00	4.04	0.07
MgO	2.05	10.02	0.00	11.82	2.46	8.87	2.42	6.92	2.44	9.40	2.82	9.61	0.00	5.35	0.00	1.68	16.50
CaO	13.98	11.84	6.68	22.40	13.73	11.67	14.09	11.65	13.51	11.95	13.43	11.80	9.37	11.97	6.60	2.69	0.03
Na_2O	0.00	1.47	8.15	0.31	0.00	1.46	0.00	1.53	0.00	0.64	0.00	1.68	6.44	1.32	7.82	0.00	0.12
K_2O	0.00	0.79	0.22	0.00	0.00	0.75	0.00	1.32	0.00	0.46	0.00	0.90	0.08	1.12	0.06	0.10	0.07
Total	99.73	99.69	99.83	99.85	99.67	99.84	99.88	99.98	99.68	99.73	99.69	99.97	99.72	99.94	99.68	99.75	99.87
Formula coefficients																	
Si	3.025	6.455	2.668	1.963	3.019	6.401	3.018	6.343	2.989	7.087	3.006	6.339	2.547	6.160	2.683	2.992	2.639
Ti	0.008	0.120	0.000	0.005	0.006	0.134	0.006	0.025	0.006	0.059	0.016	0.133	0.000	0.008	0.000	0.000	0.007
Al	1.937	2.190	1.296	0.100	1.931	2.427	1.937	2.291	1.971	1.286	1.938	2.238	1.423	2.799	1.303	1.995	2.750
Fe	1.444	2.046	0.003	0.332	1.471	2.105	1.436	2.769	1.484	2.464	1.501	2.126	0.013	2.800	0.017	2.043	2.305
Mn	0.165	0.027	0.000	0.008	0.128	0.017	0.133	0.039	0.123	0.061	0.078	0.024	0.000	0.046	0.000	0.276	0.006
Mg	0.240	2.162	0.000	0.664	0.288	1.915	0.283	1.533	0.286	2.043	0.331	2.081	0.000	1.187	0.000	0.202	2.290
Ca	1.181	1.838	0.318	0.904	1.158	1.812	1.185	1.855	1.139	1.868	1.131	1.838	0.451	1.911	0.316	0.492	0.003
Na	0.000	0.412	0.702	0.022	0.000	0.410	0.000	0.440	0.000	0.182	0.000	0.474	0.561	0.380	0.678	0.000	0.022
K	0.001	0.147	0.012	0.000	0.000	0.138	0.002	0.251	0.002	0.086	0.001	0.167	0.005	0.213	0.004	0.010	0.008
Total	8.001	15.397	5.000	4.000	8.000	15.361	8.002	15.546	8.002	15.136	8.001	15.479	5.000	15.504	5.000	8.010	10.030

Table 2. (Contd.)

Components	T-31-90				T-14a												T-15	
	Dl_p		Dl_{p*}		Dl_0			Dl_s			Dl_p			Dl_{p*}			Dl_s	
	Grt	*Chl*	*Grt*	*Chl*	*Grt*	*Chl*	*Pl*	*Grt*	*Chl*	*Pl*	*Grt*	*Chl*	*Pl*	*Grt*	*Chl*	*Pl*	*Hbl*	*Pl*
	W8/1*r*	W10	W11/1*m*	W9	D4/1*c*	D31	D14	D8/1*i*	D28	50	D9/1*r*	D26	56	F20/1*m*	F22	F58	83	62
SiO_2	37.29	29.29	37.56	28.43	36.91	29.04	64.65	37.27	28.87	59.93	37.30	28.38	60.76	37.39	29.08	61.28	50.43	63.89
TiO_2	0.14	0.00	0.01	0.17	0.00	0.00	0.02	0.07	0.00	0.01	0.00	0.09	0.00	0.00	0.00	0.08	0.18	0.05
Al_2O_3	21.08	25.32	21.15	25.84	20.64	25.30	21.88	20.66	25.38	23.67	21.02	25.55	24.53	20.75	23.69	24.11	6.69	22.15
FeO	32.85	28.04	32.80	28.46	31.61	27.48	0.39	32.72	27.80	0.05	31.29	30.58	0.08	32.19	29.26	0.00	10.31	0.07
MnO	0.15	0.00	0.10	0.00	4.09	0.06	0.01	0.81	0.00	0.00	2.03	0.16	0.00	1.17	0.12	0.13	0.22	0.00
MgO	2.59	16.99	2.36	17.06	0.89	17.76	0.00	1.29	17.70	0.00	2.28	14.93	0.01	1.96	17.66	0.00	15.26	0.07
CaO	5.57	0.04	5.81	0.00	5.61	0.01	2.96	6.67	0.00	4.94	5.97	0.07	5.83	6.22	0.09	5.41	12.00	3.89
Na_2O	0.22	0.00	0.00	0.00	0.14	0.00	10.07	0.27	0.00	9.18	0.00	0.16	8.66	0.00	0.07	8.88	0.87	10.15
K_2O	0.07	0.06	0.11	0.02	0.00	0.06	0.00	0.02	0.00	0.08	0.04	0.05	0.05	0.04	0.01	0.11	0.07	0.07
Total	99.94	99.72	99.90	99.99	99.89	99.71	99.97	99.77	99.74	97.86	99.93	99.96	99.92	99.72	99.98	100.00	96.03	100.34
Formula coefficients																		
Si	2.994	2.714	3.013	2.628	2.999	2.680	2.849	3.019	2.664	2.698	2.992	2.663	2.692	3.012	2.694	2.712	7.286	2.799
Ti	0.009	0.000	0.000	0.012	0.000	0.000	0.001	0.004	0.000	0.000	0.000	0.006	0.000	0.000	0.000	0.003	0.020	0.002
Al	1.994	2.765	1.999	2.814	1.976	2.752	1.136	1.972	0.760	1.256	1.987	2.826	1.281	1.969	0.586	1.257	1.139	1.144
Fe	2.205	2.172	2.200	2.199	2.147	2.120	0.014	2.215	2.144	0.002	2.098	2.399	0.003	2.167	2.266	0.000	1.245	0.003
Mn	0.010	0.000	0.007	0.000	0.281	0.005	0.000	0.056	0.000	0.000	0.138	0.013	0.000	0.080	0.009	0.005	0.027	0.000
Mg	0.309	2.346	0.281	2.348	0.108	2.442	0.000	0.156	2.432	0.000	0.273	2.087	0.001	0.235	2.437	0.000	3.284	0.005
Ca	0.479	0.003	0.499	0.000	0.488	0.001	0.140	0.579	0.000	0.238	0.513	0.007	0.277	0.537	0.008	0.256	1.857	0.183
Na	0.033	0.000	0.000	0.000	0.022	0.000	0.860	0.042	0.000	0.801	0.000	0.029	0.743	0.000	0.013	0.761	0.244	0.862
K	0.008	0.007	0.011	0.003	0.000	0.007	0.000	0.002	0.000	0.005	0.004	0.006	0.003	0.004	0.002	0.006	0.013	0.004
Total	8.041	10.007	8.011	10.003	8.002	10.007	5.000	8.043	10.000	5.000	8.004	10.036	5.000	8.004	10.015	5.000	15.113	5.000

Table 2. (Contd.)

Components	T-15			T-17							T-50-90					
	$D1_p$		$D1_{p*}$	$D1_0$		$D1_s$		$D1_p$			$D1_s$		$D1_p$		$D1_{p*}$	
	Hbl	*Pl*	*Hbl*	*Grt*	*Chl*	*Grt*	*Bt*	*Grt*	*Chl*	*Pl*	*Grt*	*Chl*	*Grt*	*Chl*	*Grt*	*Chl*
	86	68	59	F25/2*c*	O7	F32/2*i*	F50	F34/2*r*	F36	F35	M2/1*c*	M16	M4/1*r*	M14	M8/1*m*	M18
SiO_2	43.60	61.60	46.19	37.03	24.78	36.75	39.09	36.96	29.70	64.51	37.11	26.99	36.92	33.38	36.71	34.13
TiO_2	0.39	0.00	0.44	0.16	0.00	0.00	1.58	0.00	0.00	0.00	0.00	0.12	0.00	0.22	0.09	0.14
Al_2O_3	14.47	23.54	11.98	20.68	20.70	20.80	19.14	20.68	23.68	21.56	21.02	25.59	21.36	26.89	21.04	27.40
FeO	13.66	0.06	12.68	31.46	21.82	37.45	18.57	36.68	28.53	0.99	34.28	36.57	37.80	30.81	38.84	28.85
MnO	0.39	0.02	0.26	4.12	0.07	0.02	0.04	0.00	0.00	0.00	5.09	0.03	1.03	0.10	1.10	0.00
MgO	11.03	0.01	12.26	1.37	14.23	2.56	12.42	2.87	17.75	0.02	0.89	10.32	2.19	7.46	1.52	8.58
CaO	11.05	5.48	10.72	5.12	0.00	2.28	0.02	2.54	0.03	2.78	1.39	0.01	0.43	0.26	0.38	0.30
Na_2O	1.96	9.10	1.92	0.00	0.02	0.11	0.00	0.00	0.01	9.99	0.00	0.15	0.22	0.10	0.31	0.26
K_2O	0.37	0.08	0.33	0.04	0.00	0.00	9.04	0.05	0.08	0.05	0.04	0.00	0.05	0.71	0.01	0.28
Total	96.92	99.89	96.78	99.97	81.62	99.98	99.90	99.77	99.77	99.89	99.82	99.77	99.98	93.93	99.99	99.95
Formula coefficients																
Si	6.360	2.725	6.693	2.998	2.795	2.974	2.823	2.988	2.752	2.851	3.040	2.615	3.005	3.258	3.008	3.290
Ti	0.043	0.000	0.048	0.010	0.000	0.000	0.086	0.000	0.000	0.000	0.000	0.009	0.000	0.016	0.005	0.010
Al	2.487	1.227	2.045	1.973	2.751	1.984	1.629	1.969	2.586	1.122	2.029	2.922	2.049	3.092	2.031	3.113
Fe	1.666	0.002	1.563	2.129	2.057	2.534	1.121	2.478	2.210	0.036	2.347	2.962	2.572	2.514	0.661	2.325
Mn	0.048	0.001	0.032	0.283	0.007	0.001	0.003	0.000	0.000	0.000	0.353	0.002	0.071	0.008	0.076	0.000
Mg	2.397	0.001	2.646	0.165	2.391	0.309	1.336	0.345	2.450	0.001	0.109	1.489	0.266	1.084	0.186	1.232
Ca	1.726	0.260	1.664	0.444	0.000	0.198	0.001	0.220	0.003	0.132	0.122	0.001	0.037	0.027	0.033	0.031
Na	0.554	0.780	0.539	0.000	0.004	0.018	0.000	0.000	0.001	0.855	0.000	0.029	0.034	0.019	0.049	0.048
K	0.069	0.005	0.061	0.004	0.000	0.000	0.833	0.005	0.009	0.003	0.004	0.000	0.005	0.088	0.001	0.035
Total	15.349	5.000	15.264	8.004	10.004	8.018	7.833	8.005	10.011	5.000	8.004	10.029	8.039	10.108	8.051	10.0.83

Table 2. (Contd.)

Components	T-54-90								T-23								T-25A1	
	$D1_0$		$D1_s$		$D1_p$		$D1_{p*}$		$D1_0$		$D1_s$		$D1_p$		$D1_{p*}$		$D1_s$	
	Grt	*Bt*	*Grt*	*Chl*	*Grt*	*Chl*	*Grt*	*Chl*	*Grt*	*Chl*	*Grt*	*Chl*	*Grt*	*Chl*	*Grt*	*Chl*	*Grt*	*Chl*
	W35/2*c*	W46	W34/2*i*	W47	W39/2*r*	W43	R67/2*m*	R70	F52/1*c*	F68	F54/1*i*	F69	F56/1*r*	F61	F58/1*m*	F59	F73/1*c*	F82
SiO_2	36.48	39.85	36.72	27.63	36.86	27.00	37.30	28.87	36.00	27.39	36.65	27.19	36.51	27.84	36.28	28.68	36.17	26.20
TiO_2	0.08	1.52	0.05	0.01	0.00	0.01	0.00	0.15	0.54	0.19	0.00	0.00	0.07	0.13	0.00	0.05	0.11	0.15
Al_2O_3	21.08	21.17	20.95	25.74	20.70	25.27	21.32	24.94	20.63	26.19	20.84	26.28	20.53	25.89	20.49	24.58	20.61	25.88
FeO	33.52	22.01	34.19	32.94	38.72	35.66	38.61	35.26	35.72	31.66	37.68	31.50	37.69	31.93	38.86	31.58	38.80	37.80
MnO	6.08	0.07	5.43	0.00	0.77	0.07	1.00	0.10	4.68	0.00	1.65	0.02	0.91	0.00	0.70	0.06	2.02	0.00
MgO	0.96	8.59	1.59	13.27	2.41	11.82	1.52	10.51	1.17	14.43	1.70	14.43	1.79	13.73	1.73	14.52	1.32	9.96
CaO	1.75	0.17	1.02	0.06	0.29	0.00	0.26	0.02	1.09	0.00	1.41	0.00	2.30	0.03	1.45	0.07	0.81	0.00
Na_2O	0.00	0.00	0.00	0.14	0.00	0.00	0.00	0.04	0.00	0.04	0.06	0.16	0.10	0.10	0.25	0.00	0.00	0.00
K_2O	0.02	6.38	0.04	0.05	0.05	0.02	0.00	0.11	0.00	0.003	0.00	0.00	0.02	0.13	0.02	0.21	0.00	0.00
Total	99.97	99.75	99.97	99.83	99.80	99.85	99.99	99.99	99.82	99.91	100.00	99.57	99.91	99.77	99.78	99.75	99.84	99.99
Formula coefficients																		
Si	2.982	2.865	2.995	2.623	3.004	2.590	3.043	2.787	2.956	2.575	2.987	2.565	2.976	2.636	2.973	2.710	2.967	2.538
Ti	0.005	0.082	0.003	0.000	0.000	0.001	0.000	0.011	0.034	0.013	0.000	0.000	0.004	0.009	0.000	0.004	0.007	0.011
Al	2.031	1.793	2.013	2.880	1.988	2.856	2.049	2.836	1.996	2.902	2.002	2.922	1.971	2.888	1.979	2.737	1.992	2.954
Fe	2.291	1.323	2.331	2.614	2.638	2.859	2.632	2.845	2.452	2.488	2.568	2.484	2.568	2.527	2.662	2.495	2.661	3.060
Mn	0.421	0.005	0.375	0.000	0.053	0.006	0.069	0.008	0.325	0.000	0.114	0.001	0.063	0.000	0.049	0.004	0.140	0.000
Mg	0.117	0.919	0.193	1.876	0.293	1.689	0.185	1.511	0.142	2.021	0.206	2.027	0.218	1.937	0.211	2.044	0.161	1.437
Ca	0.153	0.013	0.089	0.006	0.025	0.000	0.022	0.002	0.096	0.000	0.123	0.000	0.201	0.003	0.127	0.007	0.071	0.000
Na	0.000	0.001	0.000	0.026	0.000	0.000	0.000	0.007	0.000	0.007	0.010	0.029	0.016	0.018	0.040	0.000	0.000	0.000
K	0.002	0.585	0.004	0.006	0.005	0.002	0.000	0.014	0.000	0.003	0.000	0.000	0.002	0.016	0.002	0.026	0.000	0.000
Total	8.002	7.586	8.004	10.032	8.005	10.002	8.000	10.021	8.000	10.010	8.010	10.029	8.018	10.034	8.042	10.026	8.000	10.000

Table 2. (Contd.)

Components	T-25A1				T-25b						T-69-90					
	$D1_p$		$D1_{p*}$		$D1_0$	$D1_s$		$D1_p$		$D1_p$	$D1_0$		$D1_p$		$D1_{p*}$	
	Grt	*Chl*	*Grt*	*Chl*	*Hbl*	*Hbl*	*Pl*	*Hbl*	*Pl*	*Hbl*	*Grt*	*Bt*	*Grt*	*Bt*	*Grt*	*Bt*
	F76/1*r*	F80	F77/1*m*	F78	106	65	83	69	78	70	T57/2*c*	T55	T58/2*r*	T61	T59/2*m*	T60
SiO_2	36.38	26.48	36.48	26.85	52.12	49.50	59.70	44.27	55.42	43.46	37.54	36.64	37.28	36.41	37.11	35.25
TiO_2	0.00	0.00	0.01	0.18	0.22	0.25	0.04	0.38	0.00	0.31	0.17	1.73	0.02	1.98	0.00	1.20
Al_2O_3	20.61	25.39	20.87	26.57	4.90	8.08	24.47	15.17	26.83	15.71	21.02	19.62	20.75	19.23	21.52	20.34
FeO	37.84	38.02	38.77	36.01	10.30	11.04	0.17	13.30	0.87	13.33	33.55	27.40	39.00	28.08	38.85	29.81
MnO	1.71	0.13	1.66	0.08	0.11	0.24	0.06	0.30	0.05	0.33	2.43	0.11	0.18	0.03	0.16	0.09
MgO	1.19	9.89	0.79	10.28	16.13	13.87	0.01	10.68	1.14	10.61	0.52	5.63	0.97	5.70	0.70	5.74
CaO	1.93	0.00	1.38	0.00	12.09	12.27	5.94	11.57	7.51	11.69	4.77	0.00	1.55	0.00	1.51	0.09
Na_2O	0.05	0.00	0.00	0.00	0.47	0.81	8.17	1.26	5.93	1.29	0.03	0.20	0.25	0.25	0.12	0.15
K_2O	0.01	0.02	0.03	0.00	0.09	0.17	0.09	0.30	0.42	0.32	0.00	8.64	0.01	8.32	0.00	7.30
Total	99.72	99.93	99.99	99.96	99.43	96.23	98.65	97.23	98.17	97.05	100.03	99.96	100.01	99.99	99.96	99.98
Formula coefficients																
Si	2.982	2.570	2.992	2.587	7.463	7.206	2.687	6.415	2.529	6.317	3.052	2.773	3.056	2.754	3.038	2.631
Ti	0.000	0.000	0.000	0.013	0.024	0.027	0.001	0.041	0.000	0.034	0.011	0.098	0.001	0.112	0.000	0.067
Al	1.991	2.904	2.017	3.017	0.827	1.386	1.298	2.590	1.443	2.691	2.014	1.750	2.004	1.714	2.076	1.789
Fe	2.593	3.085	2.658	2.901	1.233	1.343	0.006	1.611	0.033	1.620	2.279	1.734	2.672	1.775	2.659	1.860
Mn	0.119	0.011	0.016	0.007	0.013	0.030	0.002	0.037	0.002	0.041	0.167	0.007	0.013	0.002	0.011	0.006
Mg	0.146	1.430	0.097	1.475	3.440	3.008	0.001	2.305	0.077	2.297	0.063	0.634	0.118	0.642	0.085	0.638
Ca	0.170	0.000	0.121	0.000	1.854	1.913	0.286	1.796	0.367	1.820	0.415	0.003	0.136	0.001	0.132	0.009
Na	0.008	0.000	0.000	0.000	0.130	0.228	0.713	0.354	0.524	0.363	0.000	0.029	0.039	0.036	0.019	0.022
K	0.001	0.003	0.003	0.000	0.016	0.032	0.005	0.05	0.024	0.059	0.000	0.834	0.000	0.803	0.004	0.695
Total	8.009	10.003	8.003	10.000	15.001	15.173	5.000	15.205	5.000	15.243	8.000	7.862	8.039	7.839	8.023	7.717

Note: Here and in Table 3:

* compositions correspond to retrograde stage $D1_{p*}$;

** garnet grain number and position of microprobe analysis: *c*—core; *i*—central zone; *r*—outer zone; *m*—rim at the contact with chlorite or biotite.

Formula coefficients are calculated: *Grt*, on 8 cations; *Chl*, on 10 cations; *Hbl*, on 13 cations, Si + Ti + Al + Fe + Mn + Mg = 13; *Bt*, on 7 cation, Si + Ti + Al + Fe + Mn + Mg = 7; *Pl*, on 5 cations; *Cpx*, on 4 cations.

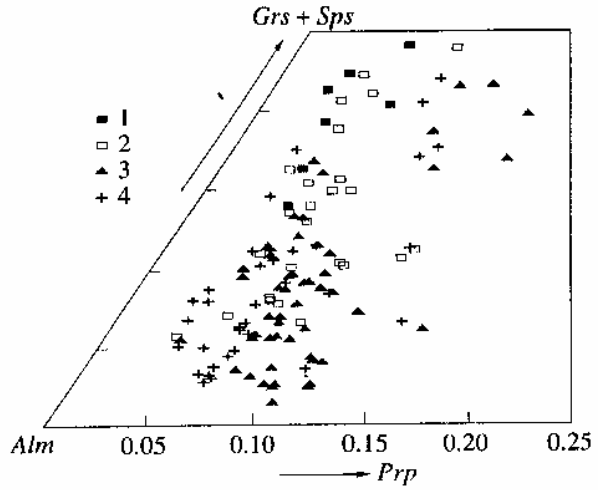

Fig. 4. Diagram of garnet compositions from the rocks of the Tumanshet zonal complex.
(1) $D1_0$; (2) $D1_s$; (3) $D1_p$ (prograde stage and metamorphic peak); (4) $D1_{p*}$ (retrograde stage).

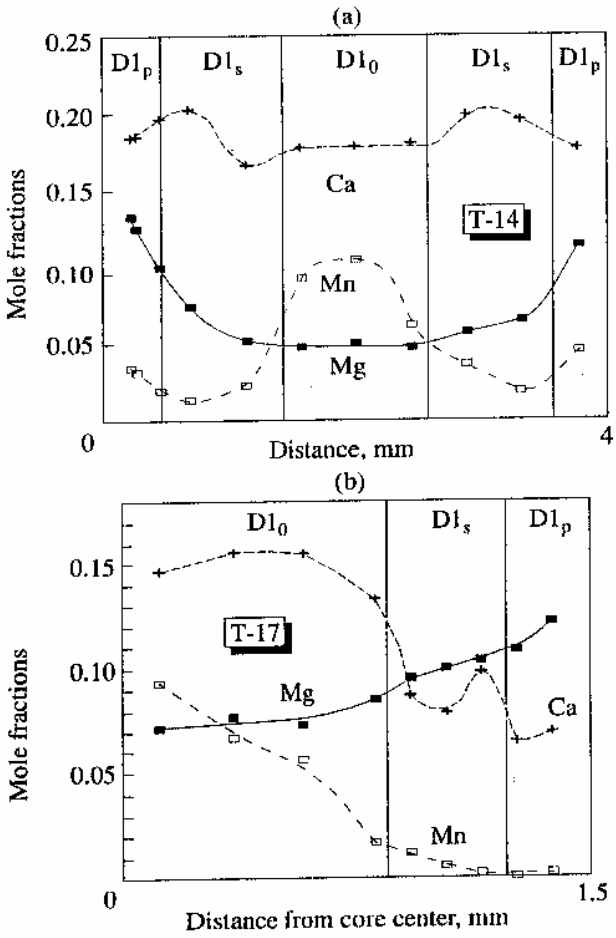

Fig. 5. Typical microprobe profiles of two garnet grains from schist Samples T-14 and T-17 (Table 1), Tumanshet zonal complex. Vertical lines separate the consequent stages of deformations within kinematic cycle D1.

Qtz at the contacts of *St* and *Bt* in Sample T-17. They resulted from the reaction *Bt* + *St* = *Chl* + *Ms* + *Qtz*, which occurred on the final stage of metamorphic evolution. Rocks of similar bulk composition from different metamorphic zones differ in their modal composition, grain size, and mineral zoning. Thus, the nucleation, growth, and disappearance of minerals and mineral assemblages were controled by a mechanism excluding the formation of reaction textures.

Fluid transport of components could be such a mechanism. Under such conditions, the minerals grew through reactions of the mineral–fluid–mineral type. Fluid abundance of rocks, direction and activity of the fluid transport, and migration paths play leading role in this process. Under nonhydrostatic pressure, hydrothermal transport proceeds toward the lower pressure rather than lower concentration. Mineral zoning results from the displacement of mineral equilibria under changing *P–T* parameters. Net-transfer equilibria lead to changes in relative mineral contents up to a change in mineral paragenesis during the evolution of metamorphic parameters (Perchuk, 1973, 1977). At $T < 700°C$, solid-state diffusion is limited because of low values of diffusivities (Gerasimov, 1992). The equilibrium of rims of contacting minerals could be attained by continuous component exchange via intergranular fluid. Only in this case will the rate of equilibration be higher than the rate of the change of external metamorphic parameters.

The character of garnet growth depends on bulk rock composition. In the garnet amphibolites of the basement, garnet forms elongated porphyroblasts up to 5 mm in size containing numerous *Hbl* and *Cpx* inclusions. In the mica schists of the zonal complex, garnet occurs as rounded grains up to 5 mm in size containing quartz and plagioclase inclusions, but no primary inclusions of Mg–Fe phases. In the quartzites of the zonal complex, garnet forms small inclusion-free grains or skeletal crystals growing along *Qtz* and *Pl* grain boundaries and containing rare *Chl* inclusions. Taking into account the metapelite paragenesis of the zonal complex and garnet composition, the main reaction of garnet formation and growth was, probably, the following: *Pl* + *Chl* + *Qtz* ⟶ fluid ⟶ *Grt* + H_2O.

Thermobarometry of Mineral Equilibria

Method of estimation of mineral equilibria in thin sections. In the absence of reaction textures, the character of divariant phase equilibria and the composition of corresponding phases have particular significance. The occurrence of several mineral generations of different composition and morphology in the rocks complicates the problem but does not make it insoluble. The results of the microstructural study, which allow us to identify the instantaneous mineral generations, help to solve the problem. It is clear that this association is stable only at given *P–T* conditions and equilibrium distribution of isomorphic components. The study of transition from one deformation stage to another

Table 3. Compositional parameters and temperatures of mineral formation on different stages of the first cycle of deformation along the traverse of the Tumanshet zonal complex

Sample number	Stage	Spot			*Grt*			*Chl/Bt*				T, °C
		*Grt***	*Chl*	*Bt*	X_{Mg}	X_{Ca}	X_{Mn}	X_{Mg}	X_{Al}	X_{Si}	X_{Ti}	
T-30-90/1	$D1_s$	T35/1*c*	T43	–	0.102	0.174	0.078	0.562	0.237	0.372	–	499
	$D1_p$	T39/1*r*	T40	–	0.112	0.163	0.027	0.569	0.238	0.375	–	511
	$D1_{p*}$	E37/1*m*	T38	–	0.120	0.152	0.028	0.586	0.239	0.374	–	511
T-31-90	$D1_s$	W1/1*c*	W1	–	0.090	0.180	0.092	0.498	0.230	0.364	–	516
	$D1_p$	W8/1*r*	W1	–	0.123	0.160	0.003	0.519	0.234	0.375	–	560
	$D1_{p*}$	W11/1*m*	W9	–	0.113	0.168	0.002	0.516	0.236	0.366	–	546
T-32-90	$D1_p$	B11/1*c*	B9	–	0.077	0.046	0.044	0.405	0.241	0.370	–	550
	$D1_p$	B12/1*r*	B6	–	0.076	0.028	0.028	0.383	0.235	0.369	–	565
	$D1_{p*}$	B3/1*m*	B4	–	0.055	0.015	0.035	0.391	0.244	0.398	–	502
	$D1_s$	B14/2*c*	–	B23	0.085	0.121	0.031	0.421	0.259	0.546	0.050	538
	$D1_{p*}$	B20/2*m*	B21	–	0.071	0.015	0.033	0.422	0.241	0.373	–	525
T-33-90	$D1_s$	T62/1*c*	T67	–	0.073	0.055	0.027	0.473	0.245	0.375	–	498
	$D1_p$	T63/1*r*	T66	–	0.095	0.039	0.016	0.454	0.248	0.378	–	556
	$D1_{p*}$	T64/1*m*	T65	–	0.069	0.024	0.021	0.464	0.241	0.378	–	494
T-14a	$D1_0$	D4/1*c*	D31	–	0.048	0.178	0.093	0.535	0.232	0.370	–	406
	$D1_0$	D5/1*c*	D3	–	0.050	0.179	0.106	0.519	0.237	0.368	–	420
	$D1_s$	D8/1*i*	D2	–	0.066	0.196	0.019	0.531	0.232	0.368	–	449
	$D1_p$	D9/1*r*	D2	–	0.115	0.178	0.046	0.465	0.239	0.372	–	585
	$D1_{p*}$	D23/1*m*	D2	–	0.101	0.199	0.026	0.470	0.234	0.368	–	555
	$D1_{p*}$	F20/1*m*	F22	–	0.098	0.183	0.026	0.518	0.215	0.364	–	518
	$D1_p$	F19/2*r*	F18	–	0.134	0.186	0.036	0.480	0.231	0.363	–	606
T-34-90	$D1_s$	B26/1*c*	B41	–	0.100	0.089	0.016	0.493	0.230	0.364	–	539
	$D1_p$	B36/1*r*	B39	–	0.105	0.078	0.007	0.432	0.232	0.367	–	590
	$D1_p$	B27/1*r*	B33	–	0.096	0.086	0.012	0.423	0.230	0.362	–	578
	$D1_{p*}$	B37/1*m*	B38	–	0.077	0.085	0.006	0.424	0.233	0.360	–	5.8
	$D1_{p*}$	B30/1*m*	B31	–	0.083	0.107	0.008	0.432	0.225	0.364	–	545
	$D1_s$	B47/2*c*	B53	–	0.070	0.117	0.014	0.460	0.231	0.365	–	499
	$D1_p$	B50/2*r*	B49	–	0.092	0.091	0.021	0374	0.237	0.366	–	610
	$D1_p$	B43/2*r*	B44	–	0.098	0.070	0.019	0.404	0.234	0.362	–	597
	$D1_p$	B51/2*m*	B52	–	0.103	0.075	0.009	0.433	0.237	0.366	–	587
T-35-90	$D1_0$	M31/1*c*	M3	–	0.038	0.136	0.089	0.488	0.240	0.370	–	401
	$D1_0$	M32/1*c*	M2	–	0.052	0.121	0.047	0.456	0.238	0.364	–	456
	$D1_p$	M36/1*r*	M3	–	0.078	0.095	0.000	0.383	0.230	0.364	–	567
	$D1_{p*}$	M37/1*m*	M3	–	0.064	0.106	0.000	0.385	0.232	0.364	–	531

Table 3. (Contd.)

Sample number	Stage	Spot			*Grt*			*Chl/Bt*				*T*, °C
		*Grt***	*Chl*	*Bt*	X_{Mg}	X_{Ca}	X_{Mn}	X_{Mg}	X_{Al}	X_{Si}	X_{Ti}	
T-30-90	$D1_s$	K24/1*c*	–	K30	0.157	0.160	0.014	0.617	0.250	0.543	0.035	523
	$D1_p$	K25/1*r*	–	K28	0.164	0.184	0.008	0.615	0.255	0.547	0.030	531
	$D1_{p*}$	K26/1*m*	–	K27	0.128	0.149	0.015	0.600	0.269	0.543	0.032	497
	$D1_s$	K15/2*c*	K23	–	0.136	0.220	0.066	0.645	0.221	0.370	–	496
	$D1_p$	K19/2*r*	K20	–	0.163	0.190	0.009	0.618	0.238	0.371	–	547
	$D1_{p*}$	K17/2*r*	K18	–	0.162	0.166	0.003	0.575	0.234	0.372	–	577
T-17	$D1_0$	O9/1*c*	O2	–	0.050	0.188	0.142	0.514	0.229	0.377	–	423
	$D1_p$	D51/1*r*	–	D4	0.145	0.072	0.000	0.539	0.255	0.541	0.031	560
	$D1_{p*}$	D50/1*m*	–	D4	0.142	0.066	0.000	0.542	0.260	0.540	0.025	554
	$D1_{p*}$	D57/3*m*	D5	–	0.147	0.065	0.000	0.586	0.214	0.365	–	549
	$D1_0$	F25/2*c*	O7	–	0.072	0.162	0.094	0.537	0.236	0.386	–	458
	$D1_s$	F31/2*i*	F39	–	0.103	0.099	0.002	0.558	0.235	0.368	–	504
	$D1_s$	F32/2*i*	–	F50	0.109	0.065	0.000	0.544	0.249	0.534	0.034	504
	$D1_p$	F34/2*r*	F36	–	0.122	0.072	0.000	0.526	0.217	0.371	–	554
T-45-90	$D1_0$	M2/1*c*	M2	–	0.069	0.175	0.129	0.600	0.239	0.369	–	422
	$D1_0$	M9/1*i*	M1	–	0.080	0.175	0.034	0.575	0.217	0.370	–	454
	$D1_s$	M3/1*i*	–	M1	0.102	0.093	0.009	0.541	0.255	0.534	0.037	494
	$D1_p$	M6/1*r*	–	M1	0.148	0.077	0.003	0.508	0.247	0.528	0.034	586
	$D1_p$	M25/1*r*	M2	–	0.159	0.060	0.001	0.503	0.220	0.371	–	627
	$D1_{p*}$	M8/1*m*	–	M7	0.139	0.060	0.000	0.502	0.243	0.523	0.029	577
T-46-90	$D1_s$	T27/1*i*	T33	–	0.131	0.103	0.002	0.616	0.238	0.373	–	507
	$D1_s$	T29/1*r*	T32	–	0.136	0.109	0.001	0.601	0.231	0.366	–	524
	$D1_{p*}$	T26a/1*m*	T26	–	0.133	0.109	0.003	0.612	0.232	0.363	–	513
T-48-90	$D1_p$	M60/1*c*	–	M6	0.101	0.046	0.016	0.335	0.268	0.550	0.033	642
	$D1_p$	M63/1*r*	–	M6	0.085	0.035	0.021	0.380	0.280	0.562	0.030	568
	$D1_p$	M64/1*m*	–	M6	0.060	0.010	0.023	0.368	0.269	0.553	0.028	514
	$D1_p$	K31/2*c*	K34	–	0.083	0.013	0.016	0.288	0.231	0.365	–	665
	$D1_p$	K32/2*r*	K33	–	0.086	0.012	0.019	0.279	0.236	0.376	–	685
	$D1_p$	K39/3*r*	–	K40	0.085	0.039	0.012	0.332	0.258	0.512	0.040	606
	$D1_p$	K35/4*r*	K36	–	0.077	0.020	0.015	0.249	0.240	0.365	–	692
	$D1_{p*}$	K38/4*m*	K37	–	0.038	0.045	0.024	0.241	0.246	0.373	–	554
T-49-90	$D1_p$	M51/1*r*	–	M4	0.104	0.008	0.006	0.371	0.284	0.574	0.040	616
	$D1_{p*}$	M49/1*m*	–	M4	0.067	0.006	0.025	0.351	0.289	0.566	0.029	546
T-50-90	$D1_s$	M2/1*c*	M1	–	0.044	0.047	0.120	0.335	0.247	0.370	–	504
	$D1_p$	M4/1*r*	M1	–	0.094	0.013	0.024	0.301	0.300	0.475	–	681
	$D1_{p*}$	M8/1*m*	M1	–	0.065	0.011	0.026	0.346	0.304	0.481	–	562

Table 3. (Contd.)

Sample number	Stage	Spot			*Grt*			*Chl/Bt*				T, °C
		*Grt***	*Chl*	*Bt*	X_{Mg}	X_{Ca}	X_{Mn}	X_{Mg}	X_{Al}	X_{Si}	X_{Ti}	
T-51-90	$D1_s$	W17/1*c*	W2	–	0.060	0.044	0.115	0.343	0.296	0.471	–	549
	$D1_p$	W20/1*r*	W2	–	0.078	0.013	0.084	0.325	0.243	0.370	–	617
	$D1_{p*}$	W22/1*m*	W2	–	0.065	0.010	0.018	0.316	0.240	0.366	–	585
	$D1_p$	W28/2*c*	W3	–	0.084	0.039	0.079	0.334	0.245	0.362	–	622
	$D1_p$	R76/2*r*	R7	–	0.117	0.010	0.017	0.339	0.242	0.374	–	699
	$D1_p$	W29/2*r*	W3	–	0.117	0.009	0.016	0.334	0.234	0.363	–	704
T-53-90	$D1_p$	M25/1*r*	M2	–	0.113	0.034	0.007	0.467	0.243	0.376	–	580
	$D1_p$	M24/1*r*	M2	–	0.112	0.039	0.004	0.461	0.249	0.396	–	582
	$D1_s$	M45/2*c*	M4	–	0.097	0.061	0.004	0.486	0.243	0.368	–	536
	$D1_p$	M42/2*r*	M3	–	0.118	0.032	0.008	0.485	0.242	0.366	–	575
	$D1_{p*}$	M36/2*m*	M3	–	0.112	0.034	0.001	0.478	0.254	0.383	–	570
T-54-90	$D1_0$	W50/1*c*	W6	–	0.045	0.037	0.193	0.409	0.241	0.366	–	462
	$D1_s$	W53/1*i*	W5	–	0.075	0.052	0.030	0.405	0.242	0.371	–	544
	$D1_p$	W55/1*r*	W5	–	0.099	0.006	0.018	0.324	0.240	0.368	–	673
	$D1_p$	W54/1*r*	W5	–	0.094	0.015	0.011	0.325	0.232	0.366	–	659
	$D1_0$	W35/2*c*	–	W4	0.049	0.060	0.141	0.410	0.285	0.560	0.035	457
	$D1_s$	W34/2*i*	W4	–	0.076	0.034	0.125	0.418	0.243	0.369	–	540
	$D1_p$	W39/2*r*	W4	–	0.100	0.009	0.018	0.371	0.239	0.363	–	629
	$D1_{p*}$	R67/2*m*	R7	–	0.066	0.008	0.024	0.347	0.245	0.390	–	563
T-23	$D1_0$	F52/1*c*	F68	–	0.055	0.036	0.108	0.448	0.243	0.364	–	468
	$D1_s$	F54/1*i*	F69	–	0.074	0.043	0.038	0.449	0.245	0.362	–	514
	$D1_p$	F56/1*r*	F61	–	0.078	0.067	0.021	0.434	0.244	0.371	–	533
	$D1_{p*}$	F58/1*m*	F59	–	0.073	0.042	0.016	0.450	0.231	0.374	–	512
	$D1_p$	D69/2*r*	D6	–	0.077	0.040	0.018	0.414	0.233	0.363	–	543
	$D1_{p*}$	D62/2*m*	D6	–	0.067	0.045	0.019	0.435	0.251	0.378	–	505
T-61-90/1	$D1_s$	R37/1*c*	R4	–	0.080	0.048	0.031	0.476	0.250	0.369	–	5141
	$D1_p$	R43/1*r*	R4	–	0.088	0.035	0.022	0.448	0.250	0.375	–	545
	$D1_{p*}$	R39/1*m*	R4	–	0.068	0.050	0.029	0.453	0.247	0.375	–	498
T-61-90/2	$D1_s$	R27/1*c*	R3	–	0.077	0.065	0.038	0.465	0.249	0.370	–	510
	$D1_p$	R31/1*r*	R3	–	0.090	0.054	0.025	0.451	0.242	0.365	–	547
	$D1_{p*}$	R28/1*m*	R3	–	0.069	0.042	0.024	0.446	0.243	0.363	–	504
T-62-90	$D1_p$	T1/1*c*	–	T11	0.088	0.063	0.029	0.446	0.266	0.539	0.030	528
	$D1_p$	T5/1*r*	T12	–	0.085	0.038	0.029	0.457	0.248	0.368	–	533
	$D1_{p*}$	T4/1*m*	T2	–	0.068	0.034	0.027	0.468	0.251	0.373	–	488

Table 3. (Contd.)

Sample number	Stage	Spot			*Grt*			*Chl/Bt*				*T*, °C
		*Grt***	*Chl*	*Bt*	X_{Mg}	X_{Ca}	X_{Mn}	X_{Mg}	X_{Al}	X_{Si}	X_{Ti}	
T-64-90	$D1_s$	R1/1*c*	R1	–	0.055	0.092	0.143	0.358	0.251	0.371	–	522
	$D1_p$	R20/1*r*	R2	–	0.070	0.090	0.034	0.349	0.255	0.374	–	575
	$D1_{p*}$	R3/1*m*	R8	–	0.040	0.066	0.022	0.362	0.257	0.381	–	471
	$D1_p$	R24/2*r*	R2	–	0.061	0.085	0.026	0.353	0.252	0.369	–	546
T-65-90	$D1_s$	R45/1*c*	R5	–	0.051	0.095	0.123	0.348	0.253	0.374	–	518
	$D1_p$	R48/1*r*	R5	–	0.055	0.114	0.061	0.343	0.250	0.367	–	535
	$D1_{p*}$	R46/1*m*	–	R5	0.047	0.097	0.069	0.349	0.293	0.550	0.016	488
	$D1_s$	R56/2*c*	R6	–	0.058	0.093	0.105	0.355	0.257	0.372	–	535
	$D1_p$	R61/2*r*	R6	–	0.064	0.090	0.077	0.358	0.257	0.375	–	551
	$D1_{p*}$	R57/2*m*	R6	–	0.041	0.114	0.069	0.353	0.255	0.376	–	481
T-66-90	$D1_s$	K66/1*c*	K6	–	0.068	0.064	0.080	0.391	0.248	0.372	–	539
	$D1_p$	K67/1*r*	K6	–	0.056	0.069	0.049	0.372	0.250	0.370	–	518
	$D1_s$	K57/2*c*	K6	–	0.075	0.054	0.101	0.380	0.250	0.371	–	563
	$D1_p$	K60/2*r*	K6	–	0.067	0.083	0.054	0.367	0.245	0.365	–	553
	$D1_{p*}$	K58/2*m*	K6	–	0.050	0.062	0.053	0.383	0.240	0.370	–	493
T-25A1	$D1_s$	F73/1*c*	F82	–	0.057	0.025	0.046	0.320	0.247	0.361	–	559
	$D1_p$	F76/1*r*	F80	–	0.053	0.058	0.039	0.317	0.243	0.362	–	548
	$D1_{p*}$	F77/1*m*	F78	–	0.035	0.042	0.039	0.337	0.256	0.371	–	468
T-25A2	$D1_s$	S60/1*c*	S69	–	0.055	0.068	0.045	0.320	0.244	0.361	–	553
	$D1_p$	S61/1*r*	S68	–	0.051	0.060	0.043	0.334	0.244	0.363	–	527
	$D1_{p*}$	S74/1*m*	S71	–	0.042	0.042	0.038	0.348	0.253	0.367	–	489
T-68-90	$D1_s$	K41/1*c*	K4	–	0.058	0.065	0.074	0.376	0.249	0.373	–	521
	$D1_p$	K56/1*r*	K4	–	0.085	0.052	0.017	0.363	0.249	0.371	–	601
	$D1_p$	K42/1*r*	K4	–	0.090	0.073	0.020	0.356	0.263	0.392	–	620
	$D1_{p*}$	K43/1*m*	K4	–	0.059	0.058	0.046	0.388	0.217	0.378	–	514
	$D1_p$	K48/2*c*	K5	–	0.075	0.068	0.022	0.386	0.253	0.368	–	559
	$D1_p$	K54/2*r*	K5	–	0.079	0.068	0.020	0.369	0.253	0.374	–	582
	$D1_{p*}$	K50/2*m*	K5	–	0.058	0.059	0.057	0.358	0.253	0.376	–	533
T-69-90	$D1_s$	T44/1*c*	T53	–	0.039	0.046	0.011	0.269	0.248	0.370	–	530
	$D1_p$	T45/1*r*	–	T56	0.041	0.049	0.007	0.250	0.268	0.539	0.038	538
	$D1_{p*}$	T47/1*m*	T48	–	0.042	0.049	0.002	0.280	0.237	0.370	–	536
	$D1_0$	T57/2*c*	–	T55	0.027	0.151	0.057	0.268	0.269	0.539	0.040	459
	$D1_p$	T58/2*r*	–	T61	0.042	0.047	0.004	0.266	0.262	0.532	0.044	531
	$D1_{p*}$	T59/2*m*	–	T60	0.031	0.046	0.004	0.256	0.263	0.512	0.026	489
T-70-90	$D1_p$	K7/1*c*	–	K1	0.062	0.099	0.038	0.331	0.258	0.534	0.041	546
	$D1_p$	K12/1*r*	–	K9	0.067	0.110	0.061	0.332	0.245	0.517	0.039	567
	$D1_{p*}$	K10/1*m*	K8	–	0.042	0.109	0.040	0.294	0.241	0.370	–	523

Note: $X_{Mg} = Mg/(Mg + Fe)$; $X_{Ca} = Ca/(Ca + Mg + Fe)$; $X_{Mn} = Mn/(Mn + Ca + Mg + Fe)$; $X_{Al} = Al/(Al + 2Mg + 2Fe)$; $X_{Si} = Si/(Si + Mg + Fe)$; $X_{Ti} = Ti/(Ti + Mg + Fe)$.

requires not only structural mineral characteristics and the character of their zoning, but also mass-balance conditions.

The zoned garnet porphyroblasts, containing numerous *Hbl* and *Cpx* inclusions, are the most informative in the *metabasites of the basement*. It was shown that such inclusions retained their composition after entrapment by a growing garnet grain at $T < 650$–700°C because of the low rates of solid-state diffusion. Tentatively, it is reasonable to assume that these small inclusions were in equilibrium with growing zones of garnet in the moment of entrapment owing to intense component exchange through *intergranular fluid*. Microprobe analyses of inclusion at different distances from a porphyroblast core allow reconstruction of the change of compositions of mineral inclusions during the growth of the garnet grain.

Most of *the metapelites from the zonal complex* contain large garnet porphyroblasts without inclusions of Fe–Mg minerals. The garnet grains are appreciably larger than other phases. In such cases, the microstructural study was applied to identify the tendencies of changes in mineral compositions with time (Audren and Triboulet, 1993). The successive mineral generations differing in their time of formation relative to deformation stage D1 were distinguished. Within the garnet porphyroblasts, such generations correspond to different zones (Figs. 3b, 3d). If there are no porphyroblasts with inclusions of Fe–Mg minerals, the "coupling" of mineral compositions by the method "core–rim" (Perchuk, 1973; Perchuk *et al.*, 1983) may be used. If microstructural data show simultaneous mineral growth, but the minerals are separated by matrix phases, another approach may be applied. Microprobe profiles are obtained through two adjacent grains in the matrix. In the case of ideal Fe–Mg distribution, temperature may be linearly interpolated with the distribution coefficient. Thus, the interpretation of temperature includes

(a) the identification by the graphic method of the main tendencies of joint changes in phase compositions, and

(b) the calculation of a plot for the temperature change during garnet grain growth across the chemical zoning.

Such a method was successfully applied to determine the equilibrium biotite, garnet, and cordierite compositions in the products of hydrothermal experiments on geothermometer calibration (Perchuk and Lavrent'eva, 1983; Perchuk *et al.*, 1983). The method provides more complete information on temperature changes and avoids errors related to random variations of inclusion compositions (for example, because of the presence of secondary generations).

Using Mg-numbers of minerals in the *centers* and *rims* of grains with selective verification of possible equilibrium compositions by the analytical data (Table 2), the dependence of $\ln K_D$ on temperature is obtained

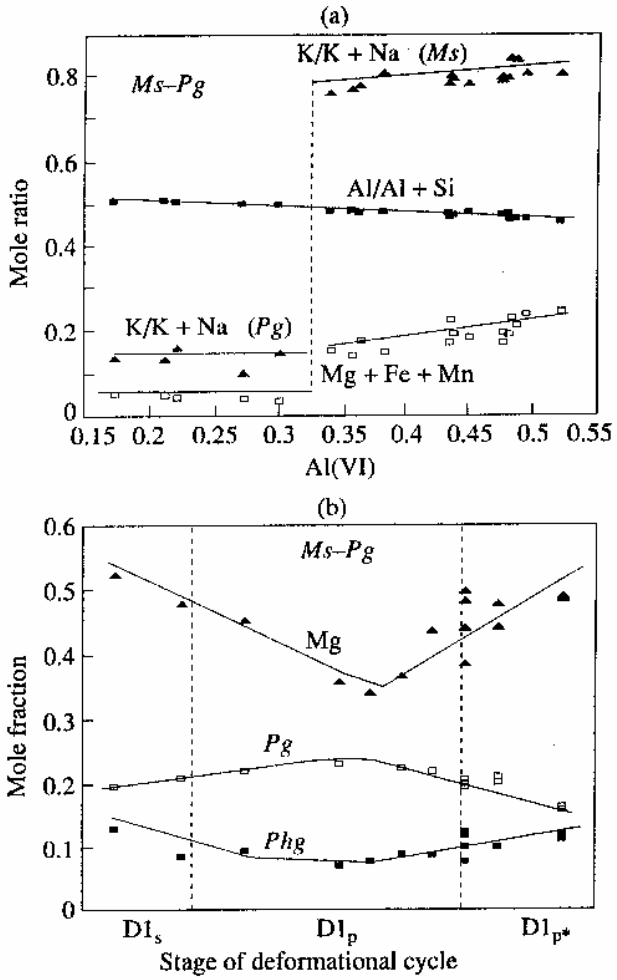

Fig. 6. Variations in white mica compositions from the rocks of the Tumanshet zonal complex on different stages of the main deformation cycle.

from the equation of the chlorite–garnet geothermometer (Perchuk, 1989b). The simultaneous mineral generations within a single lamina or microlithon were used for thermometry. The compositions of the earliest mineral generations were analyzed away from garnet grains, but within the same lamina. It allowed us to avoid errors related to composition change during fluid transport toward the growing garnet grain. For the thermometry of the later garnet generation, the compositions of close, but not contacting, mineral grains of the same generation were used. The compositions of minerals from different generations were considered as equilibrium if the later generation replaced the earlier one. The character of chemical zoning has been taken into account in such cases, as it should unambiguously show regular changes in composition during the replacement within a given deformation cycle. Most of such cases allowed several subsequent estimates of metamorphic temperature. The most typical example of temperature increase during the $D1_0$ and $D1_p$ stages at

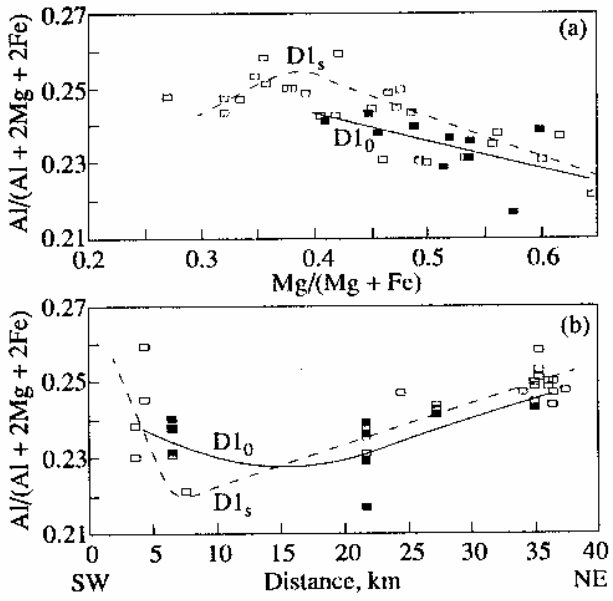

Fig. 7. Variations of chlorite compositions in the rocks of the zonal complex on different stages of the main kinematic cycle (traverse along the Tumanshet River).

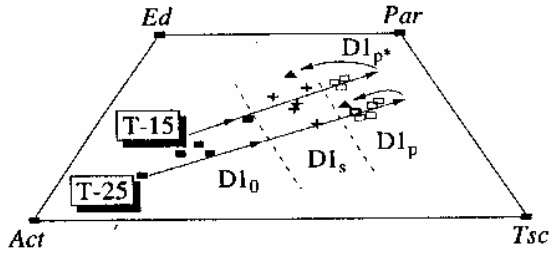

Fig. 8. Variations in amphibole compositions in two samples (Sample T-15 and Sample T-25, see Table 1) from the Tumanshet zonal complex on different stages of the main kinematic cycle.

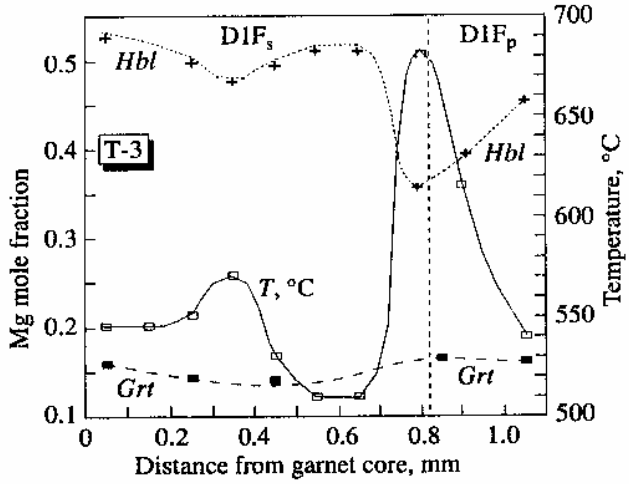

Fig. 9. Typical microprobe profile through a garnet grain from Sample T-3 (Table 3), collected from the rocks of the greenstone belt at the southwestern contact of the Tumanshet zonal complex.

Vertical lines separate consequent stages of deformations within cycle D1F.

mutual change in Mg-numbers of coexisting chlorite and garnet is shown on Fig. 10a. However, the regular change of garnet composition within an individual porphyroblast is rare. It is related to nonuniform development of deformations on the early stages of metamorphism. As a result, previously broken (and/or separated) garnet grains grow together as a single inhomogeneous porphyroblast.

Samples T-23 and T-31-90 (Table 1) containing large (up to 1 mm) adjacent porphyroblasts of *Chl* and *Grt* (Figs. 3b, 11) are the examples. Microstructural features suggest their simultaneous growth during the D1 deformation cycle. Figure 12 shows compositional changes of garnet and chlorite porphyroblasts along the microprobe profiles. The picture shows zoning in Mn and Ca as well as peculiar zoning in Mg. Similar oscillation zoning was recently described by Perchuk and Varlamov (1995) in garnets from the Caucasian eclogites; these authors suggested a mechanism of its formation. In order to confirm the oscillation patterns in N_{Mg}^{Grt}, the backscattered image of a garnet grain from Sample T-31-90 was obtained. Figure 13 shows the character of garnet heterogeneity with respect to Fe content. The change in N_{Mg}^{Grt} is apparently not occasional and should be considered in thermometry, as is evident from Fig. 10b, where the porphyroblast has finished its formation on latest stage $D1_{p^*}$ of kinematic cycle D1. The temperature curve is symmetrical. However, the use of Mg-numbers from the relict parts of the porphyroblasts (lighter parts of the grain on Fig. 13) results in the erroneous oscillation of the temperature curve (dashed line on Fig. 10b).

The microstructural study is especially useful for the thermometry of garnet-free metabasites (Triboulet and Audren, 1988). The successive generations of amphibole and plagioclase should be first identified, and their chemical zoning should be studied in microprobe profiles. The following steps include constructing the graphs of joint evolution of mineral compositions with time and their thermometric interpretation.

Chlorite–garnet equilibria as mineral thermometers and barometers. Determination of *P–T* parameters for mineral equilibria in green and blue schists is one of the most difficult problems of metamorphic petrology. Its solution provides a possibility to estimate the evolution of thermodynamic parameters from local microprobe analyses of coexisting phases. The chlorite–garnet thermometer (Perchuk, 1970), based on the exchange equilibrium

$$Chl_{Mg} + Grt_{Fe} = Grt_{Mg} + Chl_{Fe},$$

is the most effective. Recent calibrations (Perchuk, 1989b, 1990) showed the high resolution of this geothermometer, expressed in the linear equation

$$T = [3968.3 + 9P_{,}\text{kbar}]/(\ln K_D + 2.773), \quad (1)$$

where

$$K_D = [X_{Mg}/(1-X_{Mg})]^{Chl}[(1-X_{Mg})/X_{Mg}]^{Grt}, \quad (2)$$
$$X_{Mg} = Mg/(Mg+Fe+Mn).$$

The paragenesis *Chl* + *Grt* occurs in all the schists and quartzites (Table 1). Equation (1) was used to estimate the temperature of mineral equilibria on different stages of the first kinematic cycle (D1) of the evolution of the Tumanshet Complex. The thermometric results (Table 3) suggest that stage $D1_0$ is characterized by an average temperature of 456 ± 21°C, whereas for $D1_s$, temperature is appreciably higher, 529 ± 21°C. A temperature of 590 ± 44°C was obtained for stage $D1_p$, and 650–680°C was obtained for the central part of the complex. This means that the peak of metamorphism was reached during stage $D1_p$. The metamorphic regime then changed without any appreciable new deformations to a retrograde stage with an average temperature of 529 ± 33°C. Actually, the temperature evolution of the zonal complex was much more complex. The scheme on Fig. 14 shows that prekinematic stage $D1_0$ of metamorphism was approximately isothermal (Figs. 14a, 14b). Along with the S1 schistosity, deformation cycle D1 corresponded to several mineral-forming stages. The described mineral generations appeared owing to the development and extinction of a fluid–thermal anomaly at the boundary of the greenstone belt with the garnulites (Fig. 14c). These processes in the fluid–thermal anomales led to the formation of metamorphic zonation in the complex. During the latest retrograde stage of deformation cycle D1, the temperature decreased, and zonation of the complex was reduced (Fig. 14d).

The appearance of thermal anomalies always leads to the gravitational redistribution of substance within a given portion of the earth's crust. It means that the metamorphic process in zonal complexes is not only non-isothermal, but also non-isobaric. Thermal domes are never isobaric, because deep and hot substance must be "stored" in their cores. The study of the pressure evolution of a complex requires reliable geobarometers. No mineralogical barometers are available for the assemblages listed in Table 1. However, garnet and chlorite are often associated with white mica, sodic plagioclase, and quartz, which are connected by the possible reaction

$$Mg_3Al_2Si_3O_{12} + 8NaAl_3Si_3O_{10}(OH)_2 + 5Mg_5Al_2Si_3O_{10}(OH)_8 = 7Mg_4Al_4Si_2O_{10}(OH)_8 + 8NaAlSi_3O_8 + 4SiO_2$$

or

$$Prp + 8Pg + 5Cln = 7Ams + 8Ab + 4Qtz. \quad (3)$$

This reaction is useful for barometry, for it does not depend on water activity and has an appreciable volume effect, $\Delta V^0_{(3)} = 3253.6$ cal/kbar (at $T = 298$ K and $P = 1$ bar). Standard state thermodynamic data by Holland and Powell (1990) were used to compute the

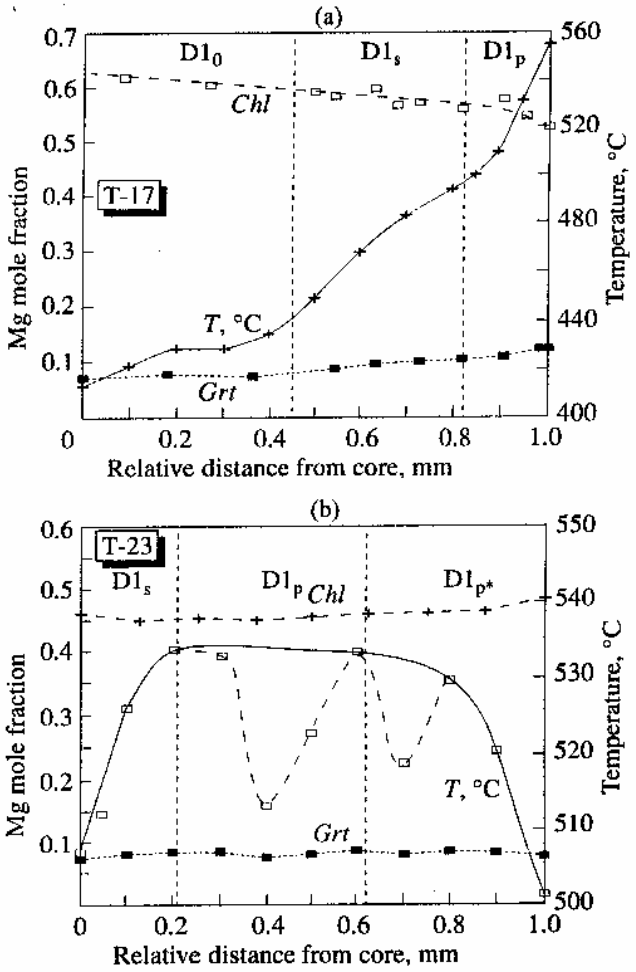

Fig. 10. Results of the garnet–chlorite thermometry of the metapelites of the Tumanshet zonal complex.
Dashed line on diagram (b) shows the temperature curve corresponding to the erroneous choice of compositions of the relict parts of garnet (see text).

monovariant line of reaction (3), which was approximated by the following linear equation:

$$\Delta G^0_{(3)} = -8999 + 5.413T + \Delta V^0_{(3)} P, \quad (4)$$

where P is pressure in kbar and T is temperature in Kelvin. Equation (4) reproduces the position of the monovariant line for reaction (3) in P–T coordinates with an accuracy of ±50 bar in a temperature interval 400–800°C.

Another mineral barometer, based on the reaction

$$Mg_3Al_2Si_3O_{12} + 2KAl_3Si_3O_{10}(OH)_2 + KMg_3AlSi_3O_{10}(OH)_2 = 6SiO_2 + 3KMg_2Al_3Si_2O_{10}(OH)_2$$

or

$$Prp + 2Ms + Phl = 6Qtz + 3East, \quad (5)$$

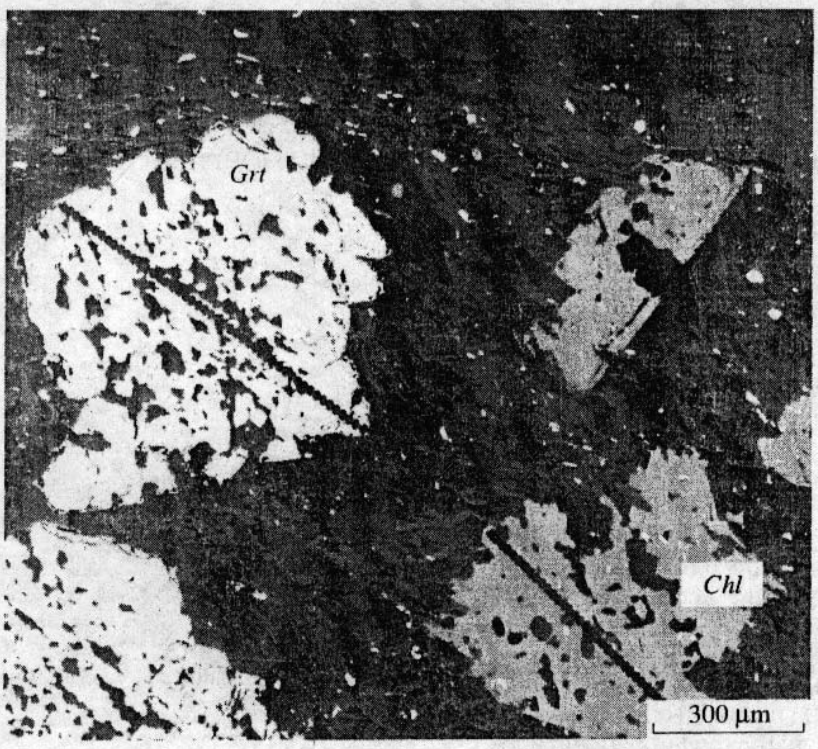

Fig. 11. Adjacent garnet and chlorite porphyroblasts growing simultaneously in the matrix of mica schist Sample T-23 during the D1 stage.
Microprobe profiles were made through these porphyroblasts along schistosity S1.

also does not depend on water activity and is characterized by appreciable volume effect, $\Delta V^0_{(5)} = 957.8$ cal/kbar (Holland and Powell, 1990). This value is sufficiently accurate at $T = 298$ K and $P = 1$ bar. However, ΔH^0 and ΔS^0 values calculated similarly to equation (4) are not consistent with other geobarometers applied to natural data. Therefore, an empirical correction for the Mg-number of biotite in equilibrium with *Prp*, *Ms*, and *Qtz* was introduced:

$$\Delta G^{T,P}_{(5)} = 11\,054 X^{Bt}_{Mg} - 13\,285 + 1.303T + \Delta V^0_{(5)} P, \quad (6)$$

where P is pressure in kbar and T is temperature in Kelvin.

Equilibrium constants of reactions (3) and (5) must include the end-member activities. However, mixing properties for some reactants are unknown. *Cln* and *Ams* activities in the chlorite solid solution, as well as *Phl* and *East* in the biotite solid solution, were calculated on the basis of a multi-site ideal model of the solid solutions (Holland and Powell, 1990):

$$RT\ln a_{Cln} = RT\ln[16(X^{M1}_{Mg})^4 X^{M2}_{Mg} X^{M2}_{Al} X^{T1}_{Al} X^{T1}_{Si}],$$

$$RT\ln a_{Ams} = RT\ln[(X^{M1}_{Mg})^4 (X^{M2}_{Al})^2 (X^{T1}_{Al})^2],$$

where

$$X^{M1}_{Mg} = Mg/(Mg + Fe),$$

$$X^{M2}_{Al} = [6 - \zeta(Fe + Mg)]/2,$$

$$X^{M2}_{Mg} = X^{M1}_{Mg}(1 - X^{M2}_{Al}),$$

$$X^{T1}_{Al} = (4 - \zeta Si)/2,$$

$$X^{T1}_{Si} = 1 - X^{T1}_{Al},$$

$$\zeta = 10/(Si + Al + Fe + Mg),$$

$$RT\ln a^{Bt}_{Phl} = RT\ln[4X^{A}_{K} X^{M1}_{Mg} (X^{M2}_{Mg})^2 X^{T2}_{Al} X^{T2}_{Si}],$$

$$RT\ln a^{Bt}_{East} = RT\ln[4X^{A}_{K} X^{M1}_{Mg} X^{M2}_{Mg} X^{M2}_{Al} (X^{T2}_{Al})^2],$$

where

$$X^{A}_{K} = K/(K + Na),$$

$$X^{M1}_{Mg} = Mg/(Mg + Fe),$$

$$X^{M2}_{Al} = [3 - \psi(Fe + Mg + Ti)]/2,$$

$$X^{M2}_{Mg} = X^{M1}_{Mg}(1 - X^{M2}_{Al}),$$

$$X^{T2}_{Al} = (4 - \psi Si)/2,$$

$$X_{Si}^{T2} = 1 - X_{Al}^{T2},$$

$$\psi = 7/(Si + Ti + Al + Fe + Mg).$$

Pg and *Ms* activities of white micas were also calculated with a multisite model, but accounting for nonideality of the solid solution (Eugster *et al.*, 1972):

$$[RT\ln a_{Pg} - G_{Pg}^{e}] = RT\ln[4X_{Na}^{A}(X_{Al}^{M2})^2 X_{Al}^{T2} X_{Si}^{T2}],$$

$$[RT\ln a_{Ms} - G_{Ms}^{e}] = RT\ln[4X_{K}^{A}(X_{Al}^{M2})^2 X_{Al}^{T2} X_{Si}^{T2}],$$

where

$$G_{Ms}^{e} = (H_{Ms}^{e} - TS_{Ms}^{e}) + PV_{Ms}^{e},$$

$$(H_{Ms}^{e} - TS_{Ms}^{e}) = (4164 + 0.395T) \times [2(X_{Na}^{A})^3 - (X_{Na}^{A})^2] + (3082 + 0.170T)[2(X_{Na}^{A})^2 - 2(X_{Na}^{A})^3],$$

$$V_{Ms}^{e} = 0.126[2(X_{Na}^{A})^3 - (X_{Na}^{A})^2] + 0.082[2(X_{Na}^{A})^2 - 2(X_{Na}^{A})^3],$$

$$G_{Pg}^{e} = (H_{Pg}^{e} - TS_{Pg}^{e}) + PV_{Pg}^{e},$$

$$(H_{Pg}^{e} - TS_{Pg}^{e}) = (3082 + 0.170T) \times [2(X_{K}^{A})^3 - (X_{K}^{A})^2] + (4164 + 0.395T)[2(X_{K}^{A})^2 - 2(X_{K}^{A})^3],$$

$$V_{Pg}^{e} = 0.082[2(X_{K}^{A})^3 - (X_{K}^{A})^2] + 0.126[2(X_{K}^{A})^2 - 2(X_{K}^{A})^3],$$

where

$$X_{Na}^{A} = Na/(Na + K),$$

$$X_{K}^{A} = 1 - X_{Na}^{A},$$

$$X_{Al}^{M2} = [2 - k(Mg + Fe)]/2,$$

$$X_{Al}^{T2} = (4 - kSi)/2,$$

$$X_{Si}^{T2} = 1 - X_{Al}^{T2},$$

$$k = 6/(Si + Al + Mg + Fe).$$

The study of metapelites showed that, along with muscovite, they always contained paragonite. This fact allows calculation of muscovite composition at given *P* and *T* within an accuracy of ±0.005 by its equilibrium with paragonite on the basis of the experimental data by Eugster *et al.* (1972):

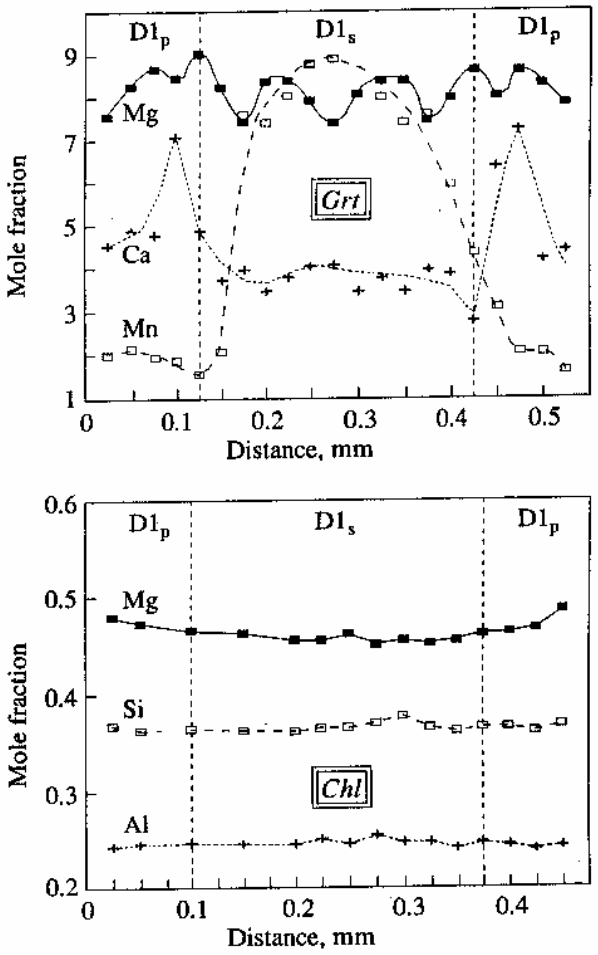

Fig. 12. Microprobe profiles through garnet and chlorite porphyroblasts (Fig. 6), which are in quasi-chemical equilibrium, in Sample T-23.

$$X_{Na}^{A}(Ms) = \exp(7.671g - 6.115 - 2.394g^2 - 1.747b + 0.08436b^2 + 2.130gb - 1.206g^2b), \quad (7)$$

where

$$g = T\,(K)/1000,$$

$$b = P\,(kbar)/10.$$

Equation (7) describes the equilibrium compositions of muscovite. Muscovite analyses from the Tumanshet zonal complex showed that Al and Si contents in the muscovite solid solution correlate linearly with paragonite content:

$$X_{Si}^{Ms} = Si/(Si + Al) = 0.57 - 0.17X_{Na}^{A},$$

$$X_{Al}^{Ms} = Al/(Al + 2Mg + 2Fe) = 0.78 + 0.52X_{Na}^{A}.$$

The calculation of the equilibrium muscovite compositions by these equations reduced significantly the errors in pressure estimates related to the incorrect

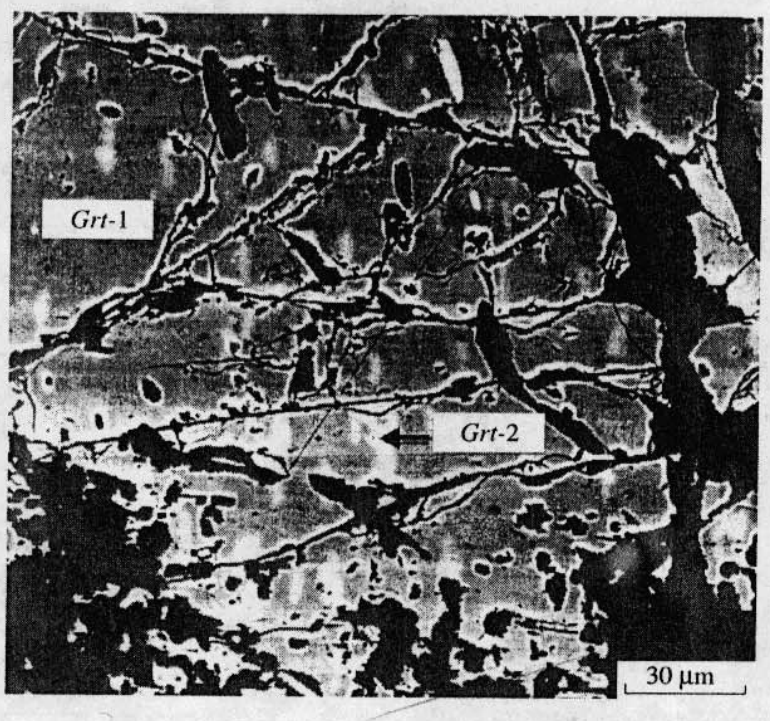

Fig. 13. Area in garnet porphyroblast from metapelite Sample T-31-90 with oscillating iron distribution in the crystal. Backscattered electron image.

choice of muscovite composition in the assemblages *Grt* + *Chl* + *Pl* + *Pg* + *Qtz* + *Ms* or *Grt* + *Bt* + *Pg* + *Qtz* + *Ms*.

The calculation of *Prp* activity accounted for the nonideal mixing of the grossular end-member in the garnet solid solution according to the regular model (Aranovich, 1983):

$$RT\ln a_{Prp}^{Grt} = 3[RT\ln X_{Mg}^{Grt} + (3300 - 1.5T)(X_{Ca}^{Grt})^2 + (5704 - 1.242T)X_{Ca}^{Grt}X_{Fe}^{Grt}], \quad (8)$$

where

$$X_{Mg} = Mg/(Fe + Mn + Mg + Ca),$$
$$X_{Fe} = Fe/(Fe + Mn + Mg + Ca),$$
$$X_{Ca} = Ca/(Fe + Mn + Mg + Ca).$$

Albite activity in plagioclase was calculated according to the sub-regular model of the solid solution (Perchuk *et al.*, 1990):

$$RT\ln a_{Ab}^{Pl} = RT\ln X_{Na} + (1980 - 1.526T) \times 2X_{Na}(X_{Ca})^2 + (6860 - 3.877T)[(X_{Ca})^3 - X_{Na}(X_{Ca})^2],$$

where

$$X_{Na} = Na/(Na + Ca),$$
$$X_{Ca} = 1 - X_{Na}.$$

Thus, pressure may be calculated from *Grt*, *Chl*, *Ms*, and *Pl* compositions in equilibrium with quartz with the equation:

$$P(\text{kbar}) = (8999 - 5.413T - G_1)/(3254 - 8000V_{Pg}^e), \quad (9)$$

where

$$G_1 = RT(7\ln a_{Ams} + 8\ln a_{Ab} - \ln a_{Prp} - 5\ln a_{Cln}) - 8[(RT\ln a_{Pg}) - G_{Pg}^e] - 8(H_{Pg}^e - TS_{Pg}^e).$$

The geobarometric equation for pressure calculation by *Grt*, *Bt*, *Ms* compositions in equilibrium with quartz, based on reaction (5) and including the correction for the Mg-number of biotite, is the following:

$$P(\text{kbar}) = (13\,285 - 11\,054X_{Mg}^{Bt} - 1.303T - G_2)/(958 - 2000V_{Ms}^e), \quad (10)$$

where

$$G_2 = RT[3\ln a_{East} - \ln(a_{Prp}a_{Phl})] - 2[(RT\ln a_{Ms}) - G_{Ms}^e] - 2(H_{Ms}^e - TS_{Ms}^e). \quad (11)$$

Empirical amphibole geothermobarometer. Amphibole occurs in metabasites of the basement and the superimposed zonal complex from greenschist to upper amphibolite facies. Its association with garnet and plagioclase is known to be a reliable mineral thermometer (Perchuk, 1989b, 1990). The association of amphibole, epidote, plagioclase, and quartz was calibrated as a geothermobarometer (Plyusnina, 1983). Many empirical and semiempirical calibrations of ther-

mometers and barometers for amphibole-bearing assemblages are known (Spear, 1993). However, all attempts to apply them to the amphibole-bearing rocks of the studied complex resulted in appreciable non-systematic inconsistencies with P–T parameters estimated in the intercalating pelites.

Amphibole is a common mineral of metabasites from greenschist facies to high-temperature amphibolites. Its composition changes regularly with metamorphic grade (Triboulet, 1992). Thermobarometry based on simple reactions including amphibole results in the problem of validity of the Gibbs phase rule for such equilibria. At constant T and P, the number of components is often significantly greater than the number of phases ($k \gg f$). This difference leads to the lack of correlation between compositions of coexisting minerals at changing temperature and pressure. The amphibole–plagioclase geothermometer by Blundy and Holland (1990) is based on the reactions

$$Ed + 4Qtz = Tr + Ab, \quad (12)$$

$$Par + 4Qtz = Hbl + Ab. \quad (13)$$

The equilibrium constants of these reactions are

$$K_{(12)} = K_{(13)} = X_{Ab}[27(\mathrm{Si} - 4)]/[256(8 - \mathrm{Si})],$$

where Si is the silica content of amphibole calculated on 13 cations and X_{Ab} is the albite mole fraction of plagioclase. Such an equilibrium constant implies the positive correlation of silica content of amphibole with anorthite content of coexisting plagioclase. The diagram in Fig. 15 shows that amphiboles formed at the peak of metamorphism in rocks of different bulk composition from the southern Brittany (France) have similar compositions which do not correlate with the composition of coexisting plagioclase. Similar results (Fig. 16) were obtained from the analysis of $\ln K_{(12)}$ dependence on the composition of coexisting plagioclase presented by Blundy and Holland (1990). These authors were forced to use an artificial correction for the excess energy of albite in their empirical calibration of the amphibole–plagioclase geothermometer.

No attempts to improve existing versions of amphibole geothermobarometers were successful. However, the empirical dependencies of Al content on pressure and Si content on temperature for hornblende from any mineral paragenesis including plagioclase and quartz were recognized. They were tested with the experimental data of Plyusnina (1983) for the assemblage $Pl + Hbl + Qtz \pm Zo \pm Chl \pm Cal$. Figure 17 shows that Si content decreases and Al content increases as temperature and pressure increase. The statistical analysis of Plyusnina's (1983) experiments showed that a reliable geothermobarometer based on amphibole composition in assemblage with *Pl*, *Qtz*, and other minerals may be formulated using these data. The statistical dependencies of amphibole composition on temperature and pressure for 48 experimental data points (Plyusnina, 1983) were best approximated by the least squares method with the following equations:

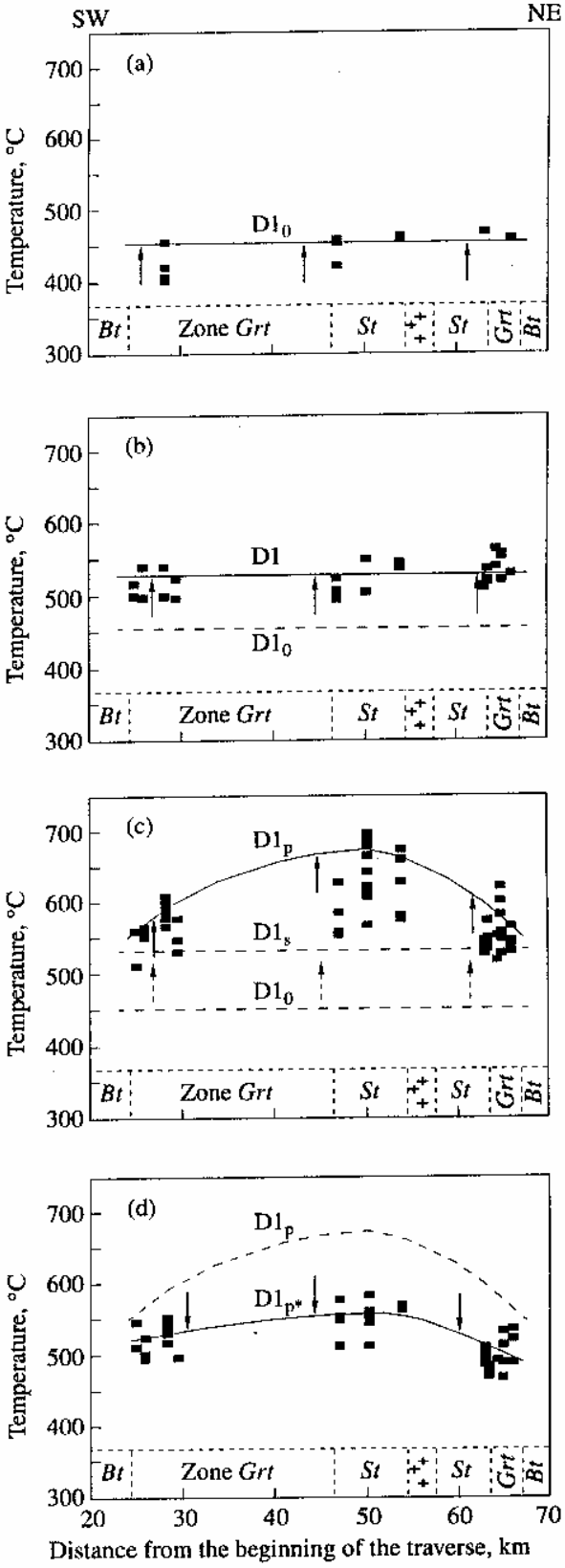

Fig. 14. Scheme of temperature evolution of the Tumanshet zonal complex at different stages of its structural history.

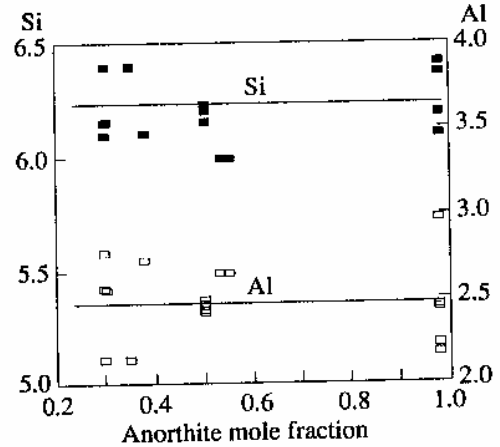

Fig. 15. Diagram illustrating the lack of correlation between plagioclase compositions and Si and Al formula values of coexisting amphibole.
Metamorphic peak in rocks of the southern Brittany (France).

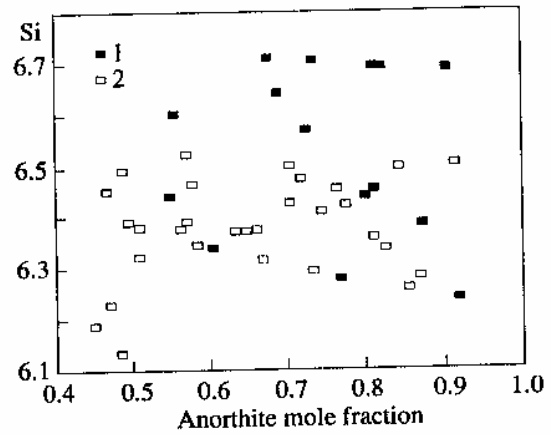

Fig. 16. Diagram illustrating the lack of correlation between plagioclase composition and Si formula value of coexisting amphiboles from the complexes Broken Hill (1) and Namaqualand (2).
The correlation of $\ln K_{12}$ with plagioclase composition from Blundy and Holland (1990) was used for calculating amphibole compositions.

$$Si^{Hbl} = 8.489 - \exp[-(6119 - 8.181T - 28.4P + 114X_{Mg}^{Hbl})/RT], \quad (14)$$

$$Al^{Hbl} = \exp[-(2543 - 4.744T - 148.1P + 175X_{Mg}^{Hbl})/RT] - 1.433, \quad (15)$$

where $P = P$, kbar; $T = T$, K; $X_{Mg}^{Hbl} = Mg/(Fe + Mg)$, bulk Mg mole fraction of amphibole; Si^{Hbl} and Al^{Hbl} are Si and Al in amphibole calculated on 13 cations. The accuracy of experimental data approximation is shown in Fig. 18. The correction for the Mg mole fraction of amphibole is related to predominant substitution Mg $\rightleftharpoons$ Al as tschermakite and glaucophane end-members, a fact supported by correlations of Mg, Al, and Si contents in natural amphiboles (Fig. 19). The net of Si and Al isopleths (nomogram) in the P–T field for pure Mg and Fe systems is shown in Fig. 20. The figure shows that silica content is less sensitive to pressure than aluminum content at a similar negative slope of both isopleth systems. This allows the use of the derived nomogram as a thermobarometer. Equations (14) and (15) can be transformed to more convenient analytical expressions:

$$T(K) = (6119 - 28.4P + 114X_{Mg}^{Hbl})/[8.181 - R\ln(8.489 - Si^{Hbl})], \quad (16)$$

$$P(kbar) = [2543 - 4.744T + 175X_{Mg}^{Hbl} + RT\ln(Al^{Hbl} + 1.433)]/148.1. \quad (17)$$

The accuracy of T and P calculations by these equations, accounting for the experimental errors of estimates of equilibrium amphibole compositions, is ±37°C and ±1.2 kbar, respectively. Testing of the equations with different metabasic paragenesis showed their good reliability. Systematic increase in calculated P–T parameters was observed only for amphiboles in contact with garnet.

Results of Thermobarometry and P–T Paths

Basement. Figure 21a shows the P–T path of evolution of the basement rocks. This is in accord with the general evolution path of granulitic complexes (Perchuk *et al.*, 1992), but it passes at higher temperature than the evolution path of rocks of the zonal complex (compare with Figs. 21b–21e). Only an increase in P–T parameters (prograde portion of the path on Fig. 21a) during the postkinematic stage ($D1F_p$ in the basement) is preserved. The temperature reached the metamorphic peak (680°C) when reaction textures appeared around the synkinematic garnet generations (Fig. 3f). This stage of evolution was followed by the retrograde stage ($D1F_p$ in the basement) when the high-temperature assemblage *Grt + Hbl + Pl + Cpx + Qtz* was replaced by actinolite–chlorite–albite–epidote–sericite–carbonate aggregates along cracks at 400–450°C and 0.5–2.0 kbar. This last stage, however, is not marked by distinct macrostructural changes, for the metamorphic conditions of this stage were similar to the low-temperature conditions of the superimposed zonal complex.

Zonal complex. P–T paths of the Tumanshet Complex (Figs. 21b–21e) differ only in maximum temperature and pressure on the metamorphic peak, which means that at a similar P–T gradient, rocks from the central part of the complex were exhumed from deeper levels. Paragenetic analysis alone without barometry would lead to a false idea on simple thermal zonation.

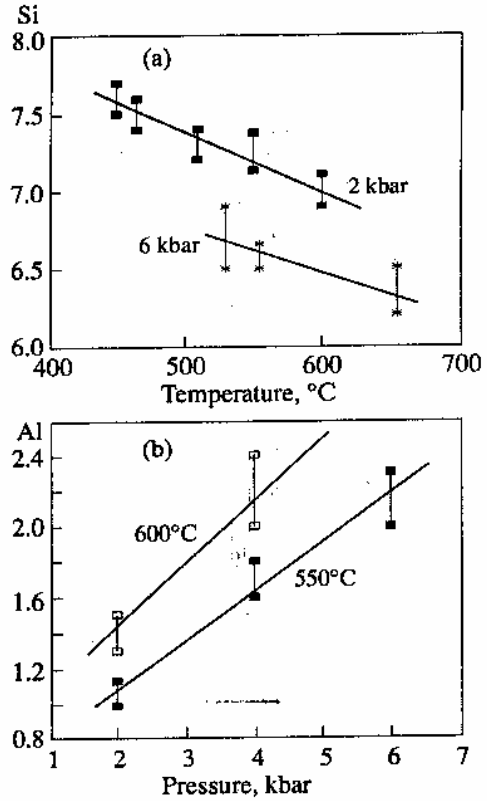

Fig. 17. Correlation of Si and Al contents of amphibole in the assemblage *Hbl* + *Pl* + *Qtz* + *Zo* + *Chl* + *Cal* with temperature and pressure according to the experimental data (Plyusnina, 1983).

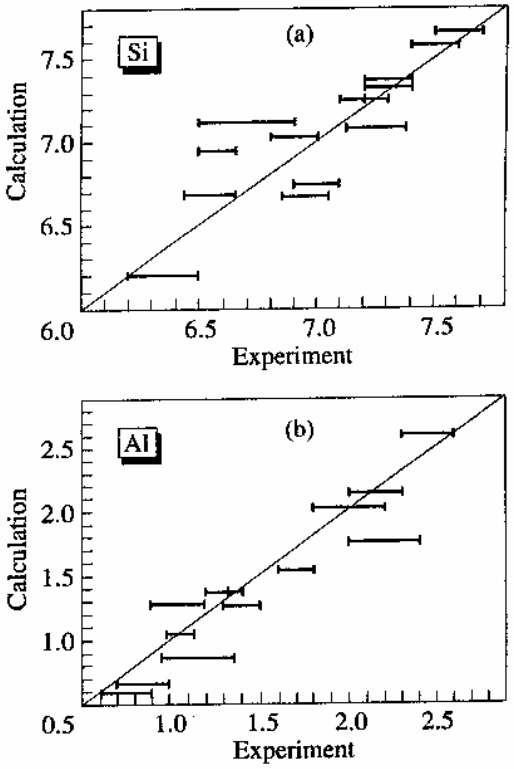

Fig. 18. Approximation of Si and Al contents of hornblende by equations (14) and (15) in comparison with the experimental data (Plyusnina, 1983).

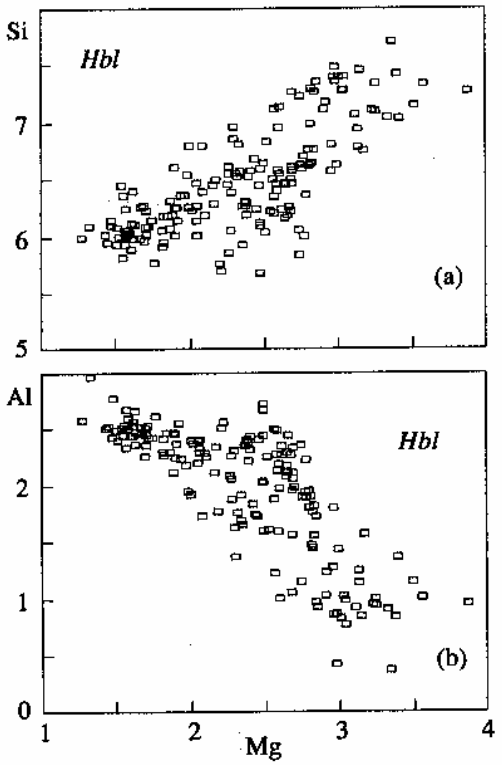

Fig. 19. Correlation of Mg with Si and Al in formulas of hornblende from the rocks of South Brittany (France).

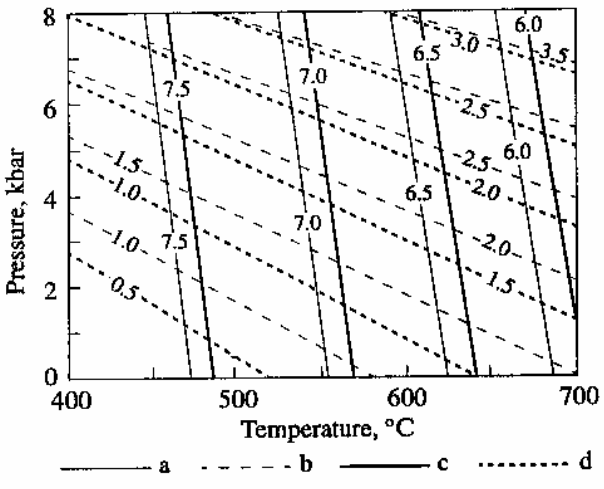

Fig. 20. Nomogram for determination of *P–T* metamorphic parameters from hornblende composition.

(a, c) Si in hornblende formulas calculated on 13 cations at $X_{Mg} = 0$ and $X_{Mg} = 1$, respectively; (b, d) Al in hornblende formulas calculated on 13 cations at $X_{Mg} = 0$ and $X_{Mg} = 1$, respectively. Calculated using equations (16) and (17).

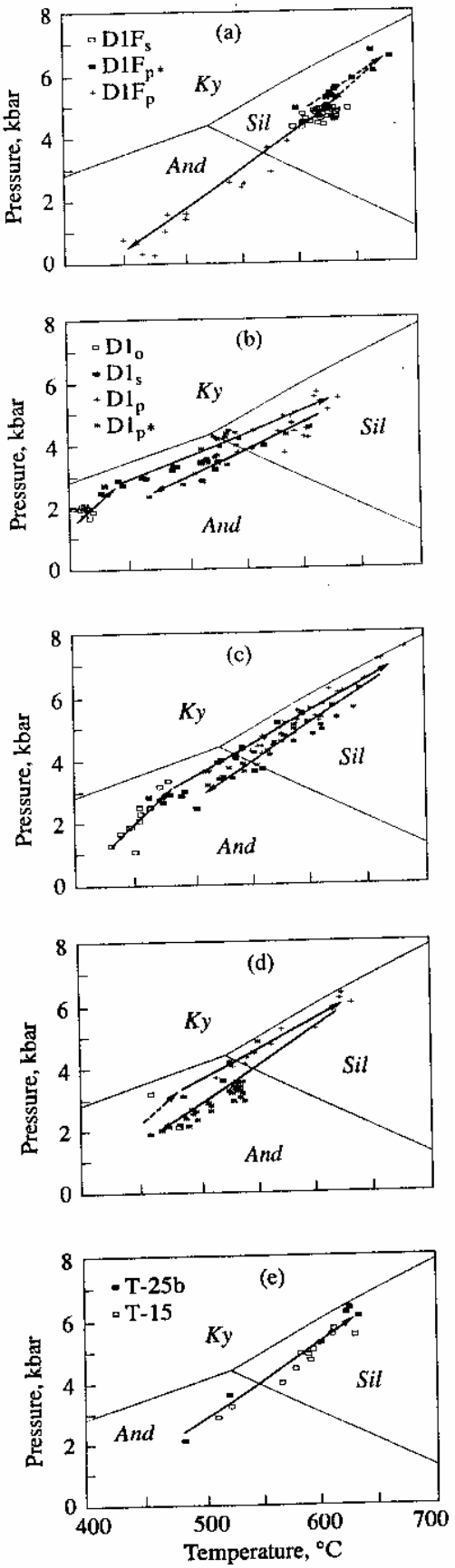

The values of temperature and pressures for the Tumanshet Complex close to the kyanite–sillimanite transition boundary support the conclusion (Sez'ko, 1988) that kyanite–sillimanite metamorphism proceeded under medium pressures.

Figures 21b–21e show that in contrast to the basement rocks, the Tumanshet Complex is characterized by a distinct prograde metamorphic stage. Up to 550°C, it corresponds to deformation stage $D1_s$ (Fig. 14b), and up to 630–680°C, i.e. the metamorphic peak, it corresponds to stage $D1_p$ (Fig. 14c). The prograde path is most thoroughly recorded in the mineral assemblages of the schists, whereas the quartzites and mica-bearing quartzites show evidence of only the retrograde path. Along with the loss of compositional features of the prograde stage, the earlier stages of deformation ($D1_0$ and $D1_s$) were also eliminated in the quartzites. Similar phenomena have been described (Aftalion *et al.*, 1991) for granulites from the Sharyzhalgai Complex, situated to the east of the studied region. The post-kinematic ($D1_{p*}$) decrease in temperature and pressure is often not recorded in the mineral associations of the schists. An important feature of the metamorphism of the zonal complex is that the prograde portion of the *P–T* trend on Fig. 21 is very close to retrograde one. This fact suggests slow descent of the complex followed by uplift at a relatively constant geothermal gradient. This conclusion is confirmed by the "tranquil" fold tectonics of the Tumanshet basin and its protoplatform character (Sez'ko, 1988). It is interesting that no schistosity or lineation were formed in the rocks within the interval 550–600°C (stage $D1_p$) of the prograde metamorphic stage, which suggests a *P–T* threshold of disappearance of notable stress and related deformations under the conditions of slow burial.

GEODYNAMIC INTERPRETATION

In choosing a geodynamic model for the formation of the Tumanshet zonal complex, we started from the following facts:

1. The Tumanshet basin shows a stratigraphic unconformity with the thick Archean basement and is situated on the boundary of the greenstone belt with gneiss–migmatite–garnulite complex (Fig. 1). Accord-

Fig. 21. *P–T* trends of evolution of metamorphic parameters for the greenstone belt (a) and the superimposed Tumanshet zonal complex (b–e).

(a) Sample T-3; (b) southern part of the complex, Samples T-31-90, T-14, T-39-90, T-15 (Table 1); (c) central part of the complex, Samples T-45-90, T-17, T-49-90, T-48-90; (d) northern part of the complex, Samples T-69-90, T-25b, T-70-90, T-62-90; (e) Samples T-25b and T-15.

P–T parameters were estimated by Fig. 20 (Samples T-3, T-15, T-25b) and equations (1) and (9) (Samples T-14 and T-17); for other metapelitic samples and Sample T-17 *P–T*, parameters were calculated by combinating the biotite–garnet thermometer (Perchuk, 1989b) and equation (10).

ing to thermobarometry and metamorphic zonation, the axis of temperature and pressure maxima coincides with the central part of the basin. It also coincides with a large gravity step, on the basis of which the deep-seated fault separating the greenstone belt and the gneissic complex is recognized (Sez'ko, 1990, 1997). This direction coincides with the elongation of the Tumanshet Complex and the orientation of lineation L1 and fold axes P2–P3. Thus, the boundary between the greenstone belt and the gneissic complex plays a key role in the development of the basin.

2. The structure of the Tumanshet basin is characterized by relatively tranquil folding, predominant box folds (D3), and weak fault tectonics. Owing to this, the marker layers were traced along the whole complex (Fig. 1).

3. Metasedimentary rocks are sharply predominant over metavolcanic rocks in the Tumanshet basin, which is indicative of the tranquil protoplatform regime of deposition.

4. The basement of the Tumanshet Group is composed of silica-rich rocks—arkose sandstones and monomineral quartzites. We suggest that in the beginning of the basin formation, the area of intense erosion was situated near the sialic migmatite–granulite complex of the basement.

5. Under the conditions of relatively tranquil tectonics, the rocks of the Tumanshet basin were metamorphosed at depths of about 15–20 km. The accumulation of such a rock sequence is possible only at significant deflection of the crust.

6. The burial and uplift of rocks of the basin took place at a relatively constant geothermal gradient (~50 K/kbar), as suggested by similar P–T trends calculated for different parts of the complex both on prograde and retrograde stages of metamorphism. The geothermal gradient was appreciably higher than the modern continental geotherm. It indicates the long-time increase in a heat flow during the formation of the Tumanshet Complex.

7. Folding P2–P3 manifests the latest tectonic event in the zonal basin. Retrograde stage of $D1_{p*}$ metamorphism is related to this folding.

These facts form the basis of the proposed model (Fig. 22) of the tectonic evolution of the Early Proterozoic Tumanshet basin and underlying heterogeneous

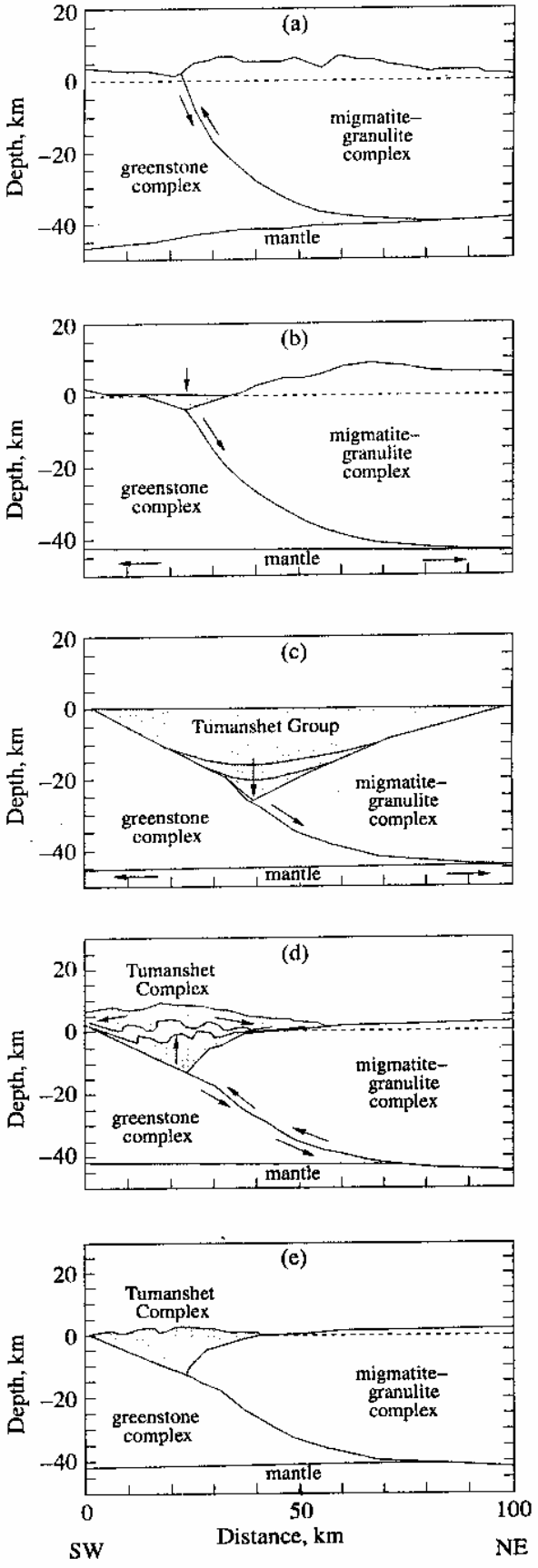

Fig. 22. Model of the geodynamic evolution of the Tumanshet zonal complex (shaded), formed on the boundary of Precambrian greenstone and granulitic complexes.

(a) Probable overthrust of granulites on the greenstone belt (deformational stage D1F in the basement rocks); (b) onset of the Tumanshet basin at the boundary between granulite and greenstone belts; (c) stage of complete deposition of sedimentary rocks and metamorphic peak in the Tumanshet basin (deformation stage D1); (d) uplift and denudation of rocks of the Tumanshet basin (stages of deformations $D1_{p*}$, D2 and D3); (e) modern position of the Tumanshet basin between granulite and greenstone belts.

Archean basement in the zone of junction of the greenstone belt and the gneiss–migmatite–granulite complex. It should be noted that deep relationships of the complexes, shown in Fig. 22, are hypothetical. However, such a kind of boundary of granulites with greenstone belts is well documented by seismic traverses in other parts of the continental crust. The Late Archean Limpopo belt in South Africa, situated between the Early Archean Zimbabwe and Kaapvaal cratons (Van Reenen and Smit, 1996), and the Late Proterozoic Lapland Complex, situated between the Archean Belomorian craton and the Inari greenstone belt (Barbey and Raith, 1991), are the best examples. The suture between granulites and cratonized rocks of the greenstone belt of Sri Lanka shows similar features (Kriegsman, 1993).

The proposed model suggests that formation of the basin and prograde metamorphism took place during crust extension (Figs. 22b, 22c) owing to convective flows in the mantle. Uplift of the Tumanshet Complex and retrograde metamorphism of the rocks resulted from crust relaxation (Fig. 22d) and gravitational redistribution of blocks with contrasting density under the basin. Lineation in the rocks of the Tumanshet zonal complex formed during the burial stage is controlled by the elongated shape of the basin and weak horizontal movements of basement blocks along the contact zone (Fig. 2). Slow uplift of the complex at relatively constant geothermal gradient was accompanied by folding and led to the exposure of the deepest parts of the complexes in the center of the basin (Fig. 22d). The highest parameters of metamorphism were reached within the basin over the contact zone of basement blocks. Crust extension and a long-term increase of heat flow as compared with the modern continental geotherm were apparently caused by intense convective flows in the mantle related to Proterozoic (~1750 Ma) influence of mantle plumes.

CONCLUSION

Structural and paragenetic study of rocks from the Tumanshet zonal complex, superimposed on the boundary of the Early Precambrian East Siberian greenstone belt and the sialic migmatite–granulite blocks of the Sayan Shield of the Siberian craton, showed the relatively simple character of its tectonic and metamorphic evolution. Its formation was controlled by the tectonic regime of these structures in the Early Proterozoic (~1750 Ma), which was reflected in the listric fault, along which the migmatite–granulite complex of the shield was displaced relative to the greeenstone belt. On the early stage of the process, a deep (15–20 km) intracontinental basin was formed in which sedimentary rocks denuded from the basement were deposited and metamorphosed. The wedge-like structure of the basin controlled the attachment of highly metamorphosed rocks to the axial zone of the lower part of the complex. In this part, the highest temperature (680°C) and pressure (7 kbar) were reached. Slow uplift of the complex at constant geothermal gradient resulted in the formation of tranquil folds and non-isobaric metamorphic zonation near the surface.

ACKNOWLEDGMENTS

The work was fulfilled under the project 3.6 SDU C.N.R.S (France) and supported by the Russian Academy of Sciences and the Russian Foundation for Basic Research (project nos. 96-05-64417 and 96-15-470).

REFERENCES

Aftalion, M., Bibikova, E.V., Bowes, D.R., Hopgood, A.M., and Perchuk, L.L., Timing of Early Proterozoic Collisional and Extentional Events in the Granulite–Gneiss–Charnockite–Granite Complex, Lake Baikal. USSR: A U–Pb, Rb–Sr, and Sm–Nd Study, *J. Geol.*, 1991, vol. 99, pp. 851–862.

Aranovich, L.Ya., Biotite–Garnet Equilibria in Metapelites. Vol. 1. Thermodynamics of Solid Solutions and End-Member Reactions, *Ocherki fiziko-khimicheskoi petrologii* (Contributions to Physico-Chemical Petrology), 1983, pp. 121–136.

Audren, C. and Triboulet, C., *P–T–t* Deformation Paths Recorded by Kinzigites during Diapirism in the Western Variscan Belt (Golfe du Morbihan, Southern Brittany, France), *J. Metamorph. Geol.*, 1993, vol. 11, pp. 337–356.

Barbey, P. and Raith, M., The Granulite Belt of Lapland, in *Granulites and Crustal Evolution*, Vielzeuf, D. and Vidal, Ph., Eds., Boston: Kluwer (NATO ASI Series), 1991.

Bibikova, E.V., Khil'tova, V.Ya., Nikitina, L.P., *et al.*, Age of the Greenstone Belts of the Sayan Region, *Dokl. Akad. Nauk SSSR*, 1982, vol. 267, no. 5, pp. 1171–1174.

Blundy, J. and Holland, T.J.B., Calcic Amphibole Equilibria and a New Amphibole–Plagioclase Geothermometer, *Contrib. Mineral. Petrol.*, 1990, vol. 204, pp. 208–224.

Bryntsev, V.V., Sumin, L.V., Ostapenko, E.I., *et al.*, Isotopic Age of the Precambrian Granitoids of the Northwestern Sayan Region, *Geol. Geofiz.*, 1985, no. 11, pp. 46–55.

Eugster, H.P., Albee, A.L., Bence, A.E., *et al.*, The Two-Phase Region and Excess Mixing Properties of Paragonite–Muscovite Crystalline Solutions, *J. Petrol.*, 1972, vol. 13, part 1, pp. 147–179.

Gerasimov, V.Yu., *Temperaturnaya evolyutsiya metamorfizma i obratimost' mineral'nykh ravnovesii* (Temperature Evolution of Metamorphic Processes and Reversibility of Mineral Equilibria), Moscow: Nauka, 1992.

Holland, T.J.B. and Powell, R., An Enlarged and Updated Internally Consistent Thermodynamic Dataset with Uncertainties and Correlations: The System K_2O–Na_2O–CaO–MgO–MnO–FeO–Fe_2O_3–Al_2O_3–TiO_2–SiO_2–C–H_2–O_2, *J. Metamorph. Geol.*, 1990, vol. 8, pp. 89–124.

Kriegsman, L.M., *Geodynamic Evolution of the Pan-African Lower Crust in Sri Lanka: Structural and Petrological Investigations into a High-Grade Gneiss Terrain*, Utrecht: Faculteit Aardwetenschappen der Universiteit Utrecht. Geologica Ultraiectina, 1993, no. 114.

Pavlovskii, E.V., On the Specific Style of the Tectonic Evolution of the Earth's Crust in the Early Precambrian, *Tr. Vost.-Sib. Geol. Inst., Akad. Nauk SSSR, Sib. Otd., Ser. Geol.*, 1962, no. 5, pp. 77–108.

Perchuk, A.L. and Varlamov, D.A., New Type of Garnet Prograde Heterogeneity, *Geokhimiya*, 1995, no. 9, pp. 1296–1310.

Perchuk, L.L., *Ravnovesiya porodoobrazuyushchikh mineralov* (Equilibria of Rock-forming Minerals), Moscow: Nauka, 1970.

Perchuk, L.L., *Termodinamicheskii rezhim glubinnogo petrogenezisa* (Thermodynamic Regime of Deep Petrogenesis), Moscow: Nauka, 1973.

Perchuk, L.L., Thermodynamic Control of Metamorphic Processes, *Energetics of Geological Processes*, Saxena, S.K. and Bhattacharji, S., Eds., New York: Springer, 1977, pp. 285–352.

Perchuk, L.L., Development of Internally Consistent Fe–Mg Geothermometers on the Basis of Nernst's Law, *Geokhimiya*, 1989, no. 5, pp. 611–622.

Perchuk, L.L., Consistency in Some Fe-Mg Geothermometers Based on Nernst's Law: Revision, *Geochem. Int.*, 1989b, vol. 12, pp. 1–11.

Perchuk, L.L., *P–T*–Fluid Regimes of Metamorphism and Related Magmatism with Specific Reference to the Baikal Lake Granulites, *Evolution of Metamorphic Belts*, Daly, S., Yardley, D.W.D., and Cliff, B., Eds., Geol. Soc. London Spec. Publ., 1989a, vol. 42, no. 20, pp. 275–291.

Perchuk, L.L., Derivation of Thermodynamically Consistent Set of Geothermometers and Geobarometers for Metamorphic and Magmatic Rocks, *Progress in Metamorphic and Magmatic Petrology*, Perchuk, L.L., Ed., Cambridge University Press, 1990, pp. 93–112.

Perchuk, L.L., Studies in Magmatism, Metamorphism, and Geodynamics, *Int. Geol. Rev.*, 1991, vol. 33, no. 4, pp. 311–374.

Perchuk, L.L., Gerya, T.V., Van Reenen, D.D., *et al.*, The Limpopo Metamorphic Complex, South Africa: 2. Decompression/Cooling Regimes of Granulites and Adjusted Rocks of the Kaapvaal Craton, *Petrology*, 1996, vol. 4, no. 6, pp. 619–648.

Perchuk, L.L. and Lavrent'eva, I.V., Experimental Investigation of Exchange Equilibria in the System Cordierite–Garnet–Biotite, *Advances in Physical Geochemistry*, 1983, vol. 3, pp. 199–239.

Perchuk, L.L., Lavrent'eva, I.V., Aranovich, L.Ya., and Podlesskii, K.K., *Biotit–granat–kordieritovye ravnovesiya i evolyutsiya metamorfizma* (Biotite–Garnet–Cordierite Equilibria and The Evolution of Metamorphism), Moscow: Nauka, 1983.

Perchuk, L.L., Podladchikov, Yu.Yu., and Polyakov, A.N., Geodynamic Modeling of Some Metamorphic Processes, *J. Metamorph. Geol.*, 1992, vol. 10, pp. 311–318.

Perchuk, L.L. and Ryabchikov, I.D., *Fazovoe sootvetstvie v mineral'nykh sistemakh* (Phase Correspondence in Mineral Systems), Moscow: Nedra, 1976.

Petrova, Z.I. and Levitskii, V.I., *Petrologiya i geokhimiya granulitovykh kompleksov Pribaikal'ya* (Petrology and Geochemistry of Granite Complexes of the Baikal Region), Novosibirsk: Nauka, 1984.

Plyusnina, L.P., *Eksperimental'noe issledovanie metamorfizma bazitov* (Experimental Study of the Metamorphism of Basic Rocks), Moscow: Nauka, 1983.

Sez'ko, A.I., Main Formation Stages of the Continental Crust of the Sayan Region, in *Evolyutsiya zemnoi kory v dokembrii i paleozoe. Sayano–Baikal'skaya oblast'* (Evolution of the Earth's Crust in the Precambrian and Paleozoic. Sayan–Baikal Region), Novosibirsk: Nauka, 1988, pp. 7–41.

Sez'ko, A.I., Precambrian Geology of the Southwestern Siberian Craton and Adjacent Areas, in *Geologiya i geokhronologiya dokembriya sibirskoi platformy i ee obramleniya* (Precambrian Geology and Geochronology of the Siberian Craton and Adjacent Areas), Leningrad: Nauka, 1990, pp. 38–49.

Sez'ko, A.I. and Mekhonoshin, A.S., The Early Precambrian of the South of Eastern Siberia, in *Dokembrii Severnoi Evrazii (tezisy dokladov)* (Precambrian of North Eurasia), St. Petersburg: Inst. Geol. Geokhr. Dokembr. Ross. Akad. Nauk, 1997, p. 93.

Spear, F.S., *Metamorphic Phase Equilibria and Pressure–Temperature–Time Paths*, Washington, D.C.: Mineralogical Society of America, 1993.

Triboulet, C. and Audren, C., Controls on *P–T–t* Deformation Path from Amphibole Zonation during Progressive Metamorphism of Basic Rocks (Estuary of the River Vilaine, South Brittany, France), *J. Metamorph. Geol.*, 1988, vol. 6, pp. 117–133.

Triboulet, C., The (Na–Ca) Amphibole–Albite–Chlorite–Epidote–Quartz Geothermobarometer in the System S–A–F–M–C–N–H_2O: 1. An Empirical Calibration, *J. Metamorph. Geol.*, 1992, vol. 10, pp. 545–556.

Van Reenen, D.D. and Smit, C.A., The Limpopo Metamorphic Belt, South Africa: 1. Geological Setting and Relationship of the Granulite Complex with the Kaapvaal and Zimbabwe Cratons, *Petrology*, 1996, vol. 4, no. 6, pp. 562–570.